Extending Imaging Depth of Multiphoton Microscopy

By

Jae Won Cha
B.S., Mechanical and Aerospace Engineering
Seoul National University (2003)

Submitted to the Department of Mechanical Engineering
in Partial Fulfillment of the Requirements for the Degree of
Master of Science in Mechanical Engineering

at the
Massachusetts Institute of Technology

August 2007

Signature of Author: ____
Department of Mechanical Engineering
Aug 31, 2007

Certified by: ____
Peter T. C. So
Professor, Department of Mech[illegible] and Biological Engineering
[illegible]isor

Accepted by: _____
Lallit Anand
Chairman, Department Committee on Graduate Students

Extending Imaging Depth of Multiphoton Microscopy

By

Jae Won Cha

Submitted to the Department of Mechanical Engineering
on Aug 31, 2007 in Partial Fulfillment of the
Requirements for the Degree of Master of Science in
Mechanical Engineering

Abstract

Two-photon excitation fluorescence microscopy has capability of deep tissue imaging with biological samples. However, because of the inhomogeneity of the refractive index in biological samples, the wavefront of the excitation light is often distorted. Due to the distortion of the wavefront, the point spread function at the focal point becomes broadened resulting in degraded resolution and lower signal. With an adaptive optics system, which consists of a wavefront camera and deformable mirror, the wavefront distortion can be measured and corrected. By correcting the distorted wavefront with adaptive optics, resolution and signal level can be preserved at greater imaging depth.

Thesis Supervisor: Peter T. C. So
Title: Professor of Mechanical and Biological Engineering

Acknowledgement

First of all, I thank my thesis advisor, Prof. Peter So for his guidance, encouragement, tolerance, and trust. He gave me limitless opportunities and whenever I was faced with a difficult question, he always supported me and never hesitated to give me advice. I also thank So Lab members, Daekeun Kim for answering to all my questions, Hyuk-Sang kwon for his warm-hearted support, Euiheon Chung for his scholastic advice, Heejin Choi for his help in class, Dimitris Tzeranis for his advice for the presentation, Yang-Hyo Kim for his numerous help in the lab, Hayden Huang for his teaching to align the system, and Barry Masters for his comment for my research.

Especially I thank my wife, Min Young Yoo for her constant support and endless love and our baby who will see the world in October 2007.

The Adaptive Optics system is supported by Imagine Optic.

Table of Contents

1. Introduction 8
1. 1. Background and motivation 8
1. 1. 1. Basic principles and advantages of two-photon excitation microscopy 8
1. 1. 2. Problem definition 11
1. 2. Objectives 11
2. Methods and Experimental Setup 12
2. 1. State of the art 12
2. 2. Application confocal microscope system to two-photon excitation fluorescence microscope 14
2. 2. 1. Signal discrimination 14
2. 2. 2. Confocal Microscopy 15
2. 2. 3. Experimental Setup 16
2. 2. 4. Confocal pinhole size 17
2. 2. 4. 1. Maximum pinhole size from axial resolution 18
2. 2. 4. 2. Minimum pinhole size from wavefront distortion 19
2. 2. 5. Slit detection 21
2. 3. Strong Background Noise 23
2. 4. Calibrating the wavefront camera and deformable mirror 24
2. 4. 1. Positions of the wavefront camera and the deformable mirror 24
2. 4. 2. Relation between the wavefront camera and the deformable mirror 26
2. 4. 2. 1. Calculating interaction matrix 27
2. 4. 2. 2. Calculating command matrix 27
2. 5. Closed loop control for distorted wavefront correction 28
2. 5. 1. Symmetric sample case 28
2. 5. 2. Asymmetric and Highly Scattering Sample Case 30
2. 5. 3. Initial aberration from the whole system (symmetric sample case) 32
2. 5. 3. 1. Aberration at e_1 33
2. 6. Detailed system configuration 34
3. Experiment and Result 36
3. 1. Signal loss due to spherical aberration as a function of imaging depth 36
3. 1. 1. Sample generating artificial spherical aberration 36
3. 1. 2. Result 37

3. 2. Point spread function degradation due to spherical aberration as a function of imaging depth 40
3. 2. 1. Sample generating artificial spherical aberration 40
3. 2. 2. Result 41
4. Conclusion and Future Work 44
5. References 45
6. Appendix 47
6. 1. Shark-Hartmann wavefront sensor 47
6. 2. Deformable mirror 47
6. 3. Resolution of the current system 48

List of Figures

Fig 1.1. Jablonski diagram for one-photon(a) and two-photon(b) excitation 8
Fig 1.2. Comparison of one- and two-photon excitation profiles 9
Fig 1.3. The schematic of two-photon excitation fluorescence microscopy..... 10
Fig 1.4. Wavefront distortion in inhomogeneous sample 11
Fig 1.5. Block diagram for distorted wavefront correction 11
Fig 2.1. System configuration of coherence-gated wavefront sensing..... 12
Fig 2.2. Scanning in the reference arm..... 13
Fig 2.3. Configuration of the Shark-Hartmann sensor..... 13
Fig 2.4. Back scattered signal from a sample 14
Fig 2.5. The schematic of confocal microscopy..... 15
Fig 2.6. System configuration 16
Fig 2.7. Pinhole size..... 17
Fig 2.8. Variation of I(u) against u for detector pinhole sizes 18
Fig 2.9. Maximum pinhole size 19
Fig 2.10. Minimum pinhole size..... 20
Fig 2.11. Slit detection..... 21
Fig 2.12. Variation of I(u) against u..... 21
Fig 2.13. Wavefront information passing through a slit..... 22
Fig 2.14. Numerically constructed circular area 22
Fig 2.15. Background signal reflected from the beamsplitter 23
Fig 2.16. Rotation of the beamsplitter..... 24
Fig 2.17. the wavefront camera and deformable mirror in the system..... 25
Fig 2.18. The wavefront camera and deformable mirror at conjugate planes..... 25
Fig 2.19. Wavefront detection of the wavefront camera 26
Fig 2.20. Wavefront correction of the deformable mirror 26
Fig 2.21. Interaction matrix calculation 27
Fig 2.22. Command matrix calculation..... 27
Fig 2.23. Wavefront detection with plane wave..... 28
Fig 2.24. Wavefront correction with feedback signal..... 29
Fig 2.25. Wavefront distortion with asymmetric and highly scattering sample 30
Fig 2.26. Wavefront correction with asymmetric and highly scattering sample 31
Fig 2.27. Inherent system aberration 32

Fig 2.28. Aberrations at e_1 33
Fig 2.29. Wavefront at e_1 33
Fig 2.30. System configuration 34
Fig 3.1. Signal loss experiment sample 36
Fig 3.2. Signal loss improvement 37
Fig 3.3. Aberration coefficients of uncompensated wavefront 38
Fig 3.4. Uncompensated wavefront 38
Fig 3.5. Aberration coefficients of compensated wavefront 39
Fig 3.6. Compensated wavefront 39
Fig 3.7. PSF degradation experiment sample 40
Fig 3.8. Lateral Resolution Improvement 41
Fig 3.9. Axial Resolution Improvement 41
Fig 3.10. Aberration coefficients of uncompensated wavefront 42
Fig 3.11. Uncompensated wavefront 42
Fig 3.12. Aberration coefficients of compensated wavefront 43
Fig 3.13. Compensated wavefront 43
Fig 6.1. Shark-Hartmann wavefront sensor 47
Fig 6.2. Deformable mirror 47
Fig 6.3. Several modes of the deformable mirror 48
Fig 6.4. Lateral resolution of the current system 49

1. Introduction

1. 1. Background and motivation

1. 1. 1. Basic principles and advantages of two-photon excitation microscopy

The theory of the two-photon excitation was first introduced by Maria Göppert-Mayer in 1931 [1]. In the two-photon excitation process, a fluorophore (a molecule which fluoresces) is brought to an electronically excited state by the simultaneous absorption of two photons. Each photon has approximately half the energy which is needed for the transition between the ground state and the excited state [Fig 1.1]. The similar one-photon excitation process is that a fluorophore is excited by only a single photon. This process typically requires photons in the ultraviolet, blue, or green spectral range, which can easily damage biological samples. However, the two-photon excitation process uses photons in red or infrared spectral range, which has less energy than those for the one-photon excitation process. Therefore, two-photon excitation microscopy can realize biological imaging with less photon-damaging [2].

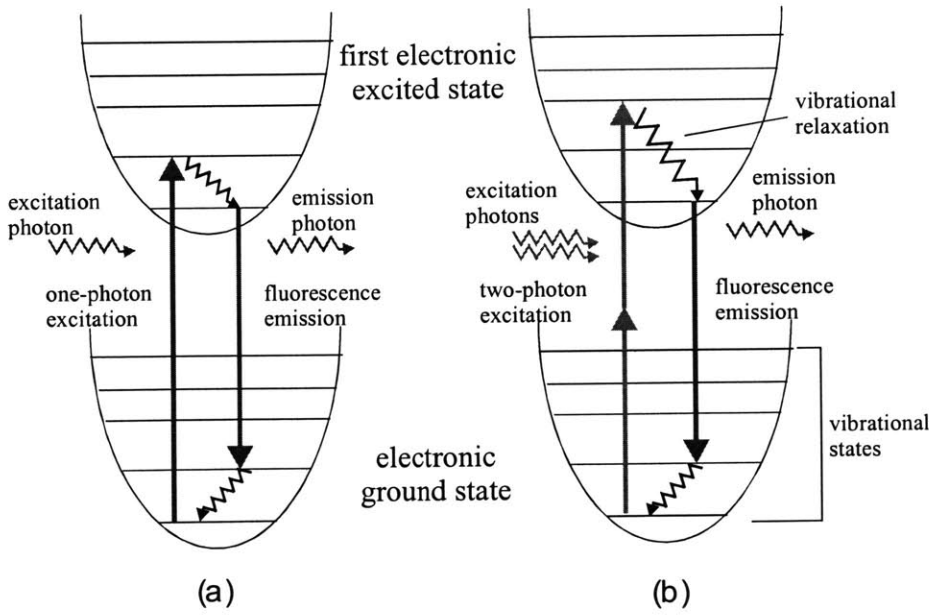

Fig 1.1. Jablonski diagram for one-photon(a) and two-photon(b) excitation

Two-photon microscopy has inherent 3D resolution due to the quadratic dependence of the excitation process on the incident light distribution. Two-photon excitation can be localized to a femtoliter region about the focal point of a high numerical aperture objective [Fig 1.2].

In addition two-photon excitation microscopy has the capability of deep tissue imaging. Because most tissues are transparent to the infrared, the infrared photons can easily penetrate the thick tissues. In the one-photon excitation microscopy, the penetration of the excitation light is limited by photon scattering and absorption.

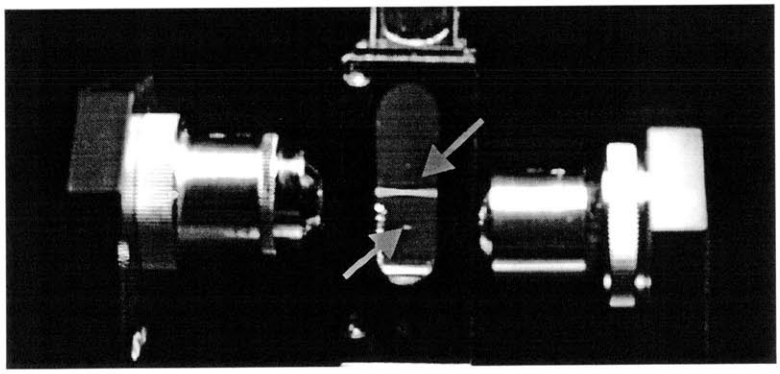

Fig 1.2. Comparison of one- and two-photon excitation profiles [2]

In 1990, Denk, Webb, and co-workers demonstrated the two-photon excitation fluorescence microscopy [3]. A critical component in the two photon excitation microscopy is its light source. Typically femtosecond pulsed laser is used. The higher peak power and the lower average power increase the efficiency of the two-photon excitation without causing a specimen thermal damage.

Fig 1.3 shows the schematic of two-photon excitation fluorescence microscopy. The raster scanning is accomplished by deflecting the excitation beam using galvanometer-driven x-y mirrors. The excitation beam is expanded by a scan lens and a tube lens to ensure overfilling of the back aperture of an objective lens. The expanded laser beam is reflected by a dichroic mirror towards the back aperture of the objective lens, and is focused on the sample. The emission signal is collected by the same objective lens and passes through the dichroic mirror. A highly sensitive photon

detector is used to detect the emission signal.

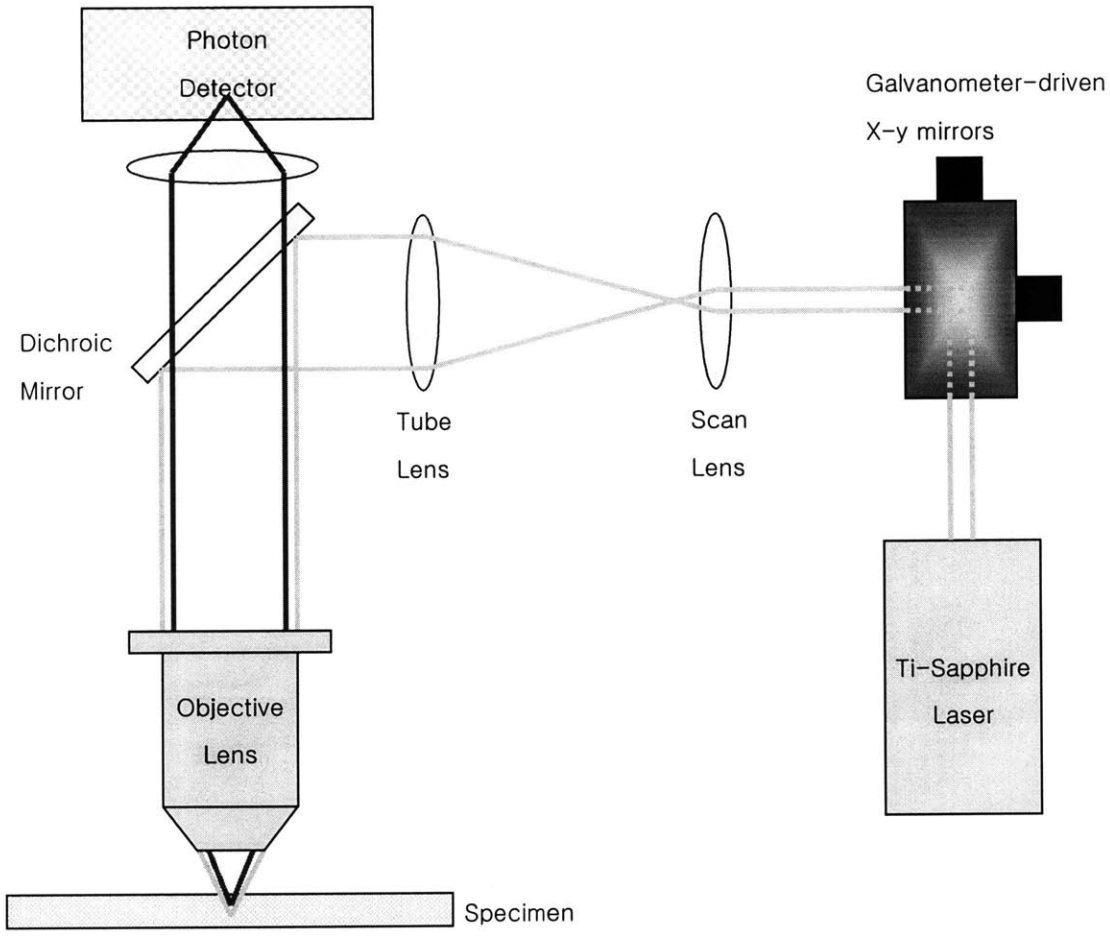

Fig 1.3. The schematic of two-photon excitation fluorescence microscopy

1. 1. 2. Problem definition

As described above, two-photon excitation fluorescence microscopy has advantages for deep tissue imaging. However, biological sample has inhomogeneous refractive indices. Because of this inhomogeneity of refractive index, the wavefront of the excitation beam is distorted [Fig 1.4]. Due to the distorted wavefront of the excitation beam, point spread function is broadened at the focal point and this leads to degraded resolution and lower signal.

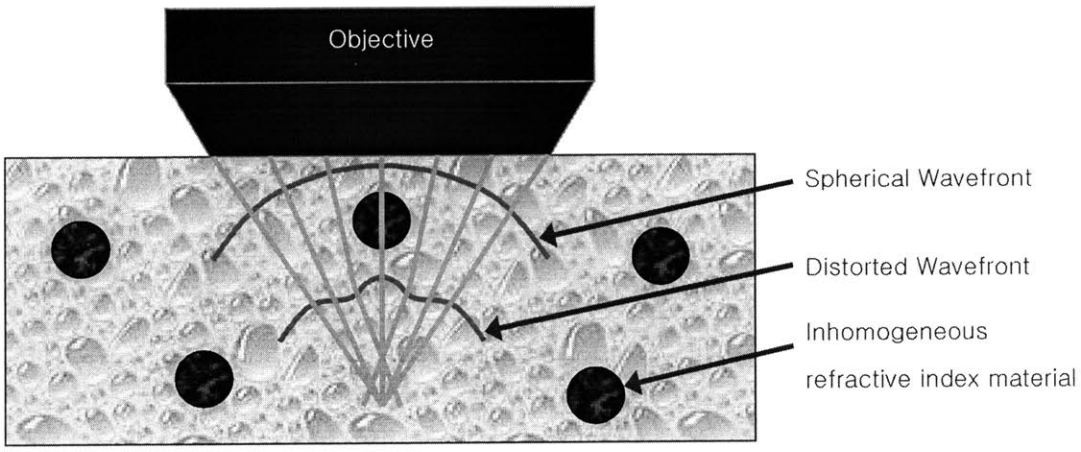

Fig 1.4. Wavefront distortion in inhomogeneous sample

1. 2. Objectives

The distorted wavefront needs to be corrected to improve resolution and increase the two-photon fluorescence signal. For the correction of the distorted wavefront, we measure the distorted wavefront using a wavefront sensor and compensate the wavefront distortion using a deformable mirror. Fig 1.5 shows the block diagram of the closed loop system for the wavefront correction.

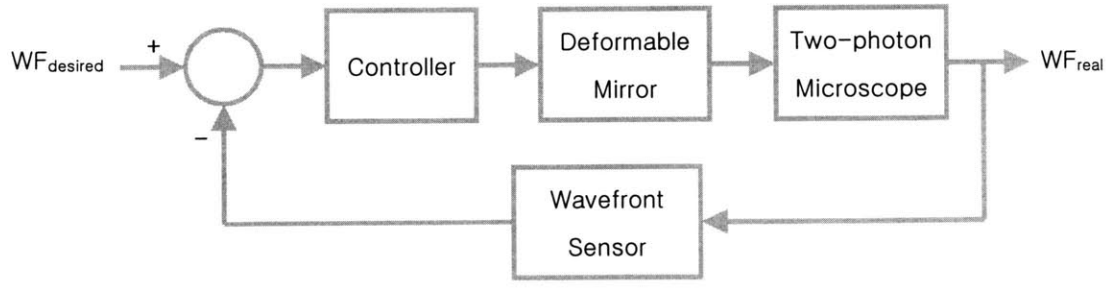

Fig 1.5. Block diagram for distorted wavefront correction

2. Methods and Experimental Setup

2. 1. State of the art

The adaptive optics has been used in various fields such as in astronomy [4] and in ophthalmology [5].

Recently the adaptive optics is applied to the two-photon excitation microscopy. In this work Markus Rueckel et al used coherence-gated wavefront sensing method [6, 7]. The coherence-gated wavefront sensing is based on optical coherence tomography (OCT). OCT uses the low temporal coherence properties of femtosecond laser pulses. Therefore, only the signal from the focal point can be picked interferometically. In the coherence-gated wavefront sensing a modified Michelson interferometer and a CCD are used to measure the distorted wavefront detection.

However, the interferometer, which is used in the coherence-gated wavefront sensing, has a complex reference arm [Fig 2.1]. In addition to being a complicated instrument, the complex reference arm may also have additional aberration due to the optical elements contained within it.

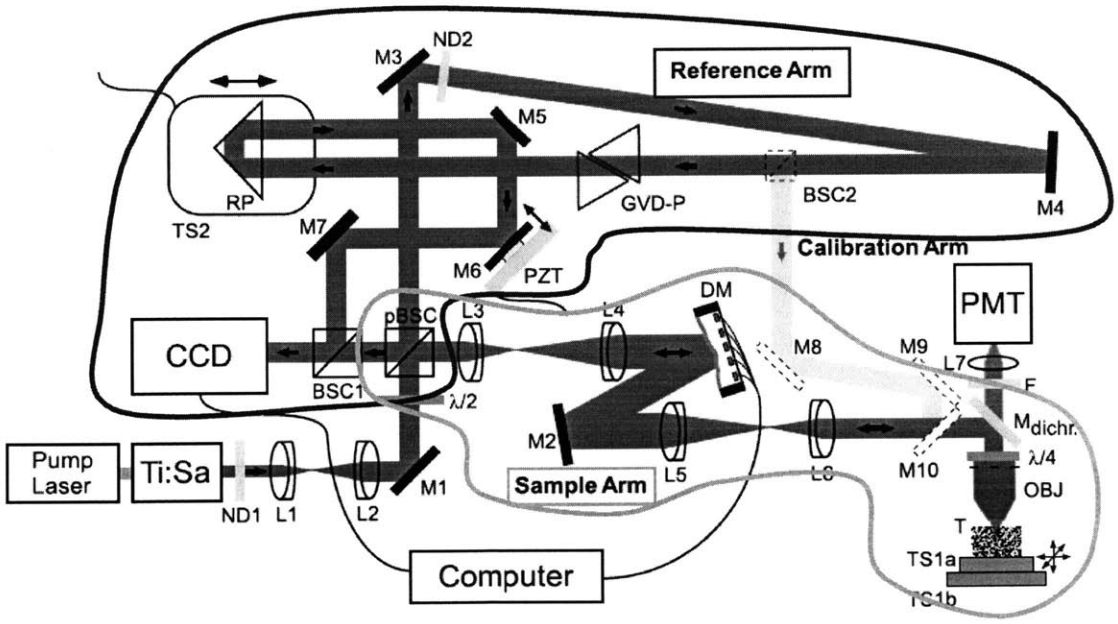

Fig 2.1. System configuration of coherence-gated wavefront sensing [7]

In addition, the interferometric method needs to scan in the reference arm to get one wavefront image. Fig 2.2 shows why the scanning is needed to make one image. Only with the image (a) the wavefront cannot be constructed because there is not enough information to determine the phase of the wavefront. With scanning in the reference arm, the phase-lead and the phase-lag can be distinguished and the wavefront can be constructed. This limits the bandwidth of the adaptive optics feedback loop.

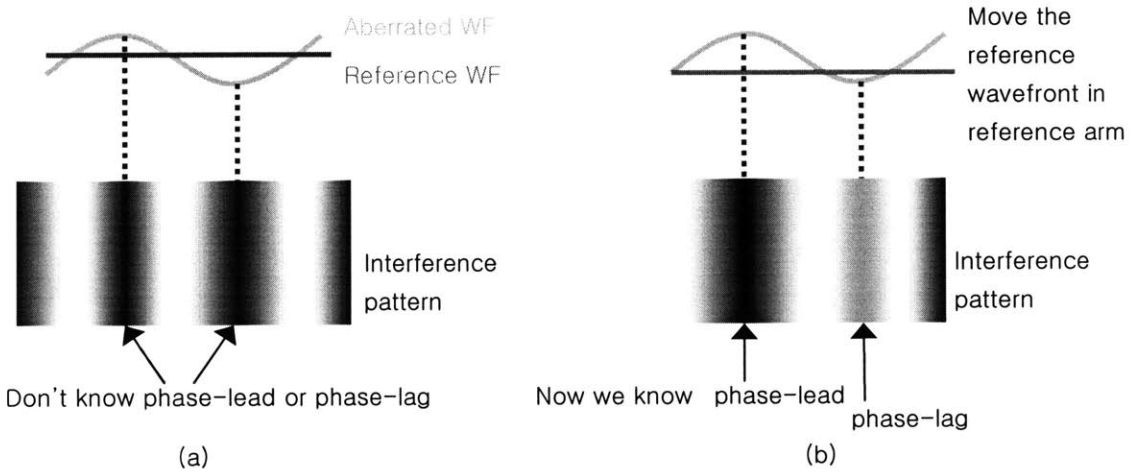

Fig 2.2. Scanning in the reference arm

To improve this inherent aberration and slow imaging, I used Shark-Hartmann sensor. Fig 2.3 shows how the Shark-Hartmann sensor works.

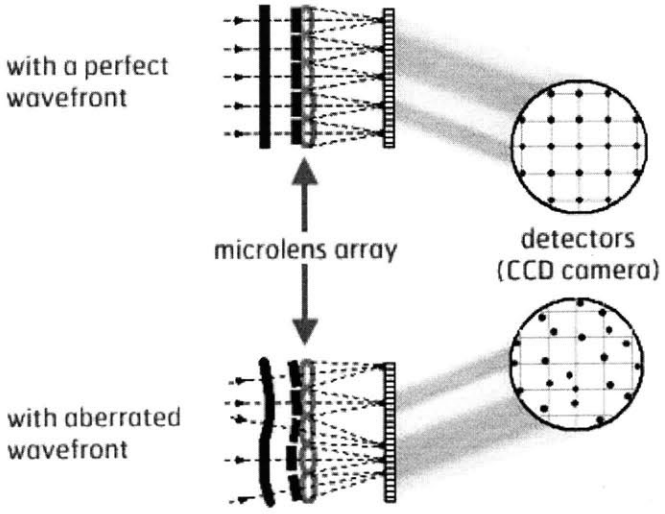

Fig 2.3. Configuration of the Shark-Hartmann sensor [8]

The Shark-Hartmann sensor has very small lenslet array. With an incident plane wave an array of foci produces a rectilinear grid defined by the lenslet dimension. However, if the incoming wavefront is distorted, the foci are displaced from the grid location. By measuring the distance of the displacement using a CCD camera, the slope of local wavefront can be calculated and the whole wavefront can be constructed.

2. 2. Application confocal microscope system to two-photon excitation fluorescence microscope

2. 2. 1. Signal discrimination

Only the aberration information of light from the focal region of the objective is relevant for optimizing two-photon excitation. However, signal does not come only from the focus, but also from out-of-focal regions [Fig 2.4]. The signal from out-of-focal regions needs to be eliminated, and we accomplished it by setting up a confocal system.

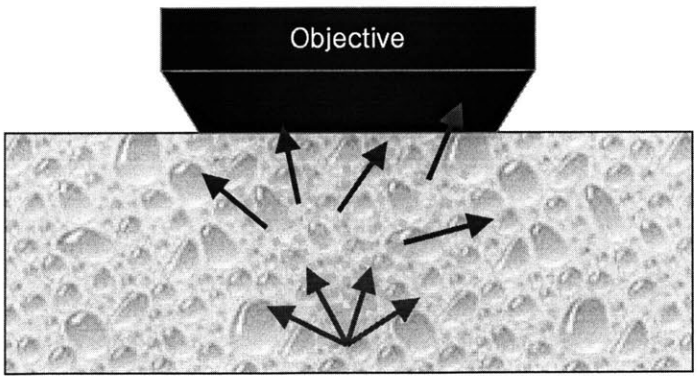

Fig 2.4. Back scattered signal from a sample

2. 2. 2. Confocal Microscopy

Fig 2.5 shows the schematic diagram of the confocal microscope.

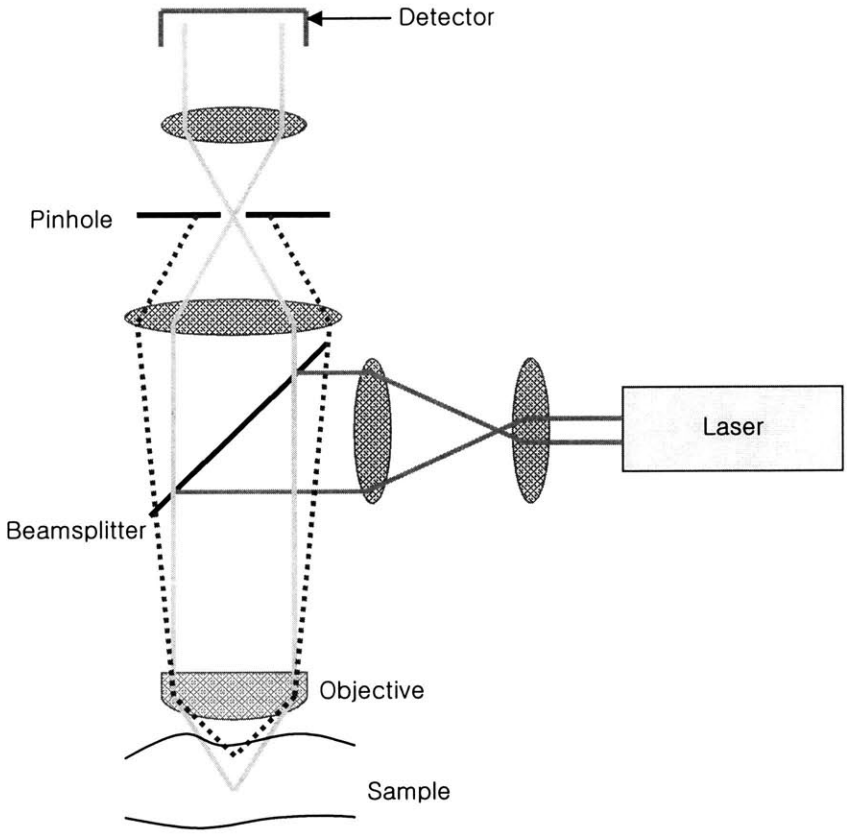

Fig 2.5. The schematic of confocal microscopy

The laser beam comes into a beamsplitter or dichroic mirror. The beam is reflected to the objective lens and focused on a sample. Signal from the sample goes back through the original beam path towards the detector. Before the detector, a pinhole is placed such that the signal originating from the focal region of the objective is focused and passes the pinhole while out-of-focus light is defocused at this plane and is blocked.

The signal can be either reflected excitation light or fluorescence. If the signal is reflected light from a sample, then the source light from a laser and the reflected light should be separated by a beamsplitter. If the signal is fluorescence light, then the beamsplitter can be replaced by a dichroic mirror. In the case of Fig 2.5, the dichroic mirror reflects the source light and passes the emission light from the sample according to the wavelength difference.

2. 2. 3. Experimental Setup

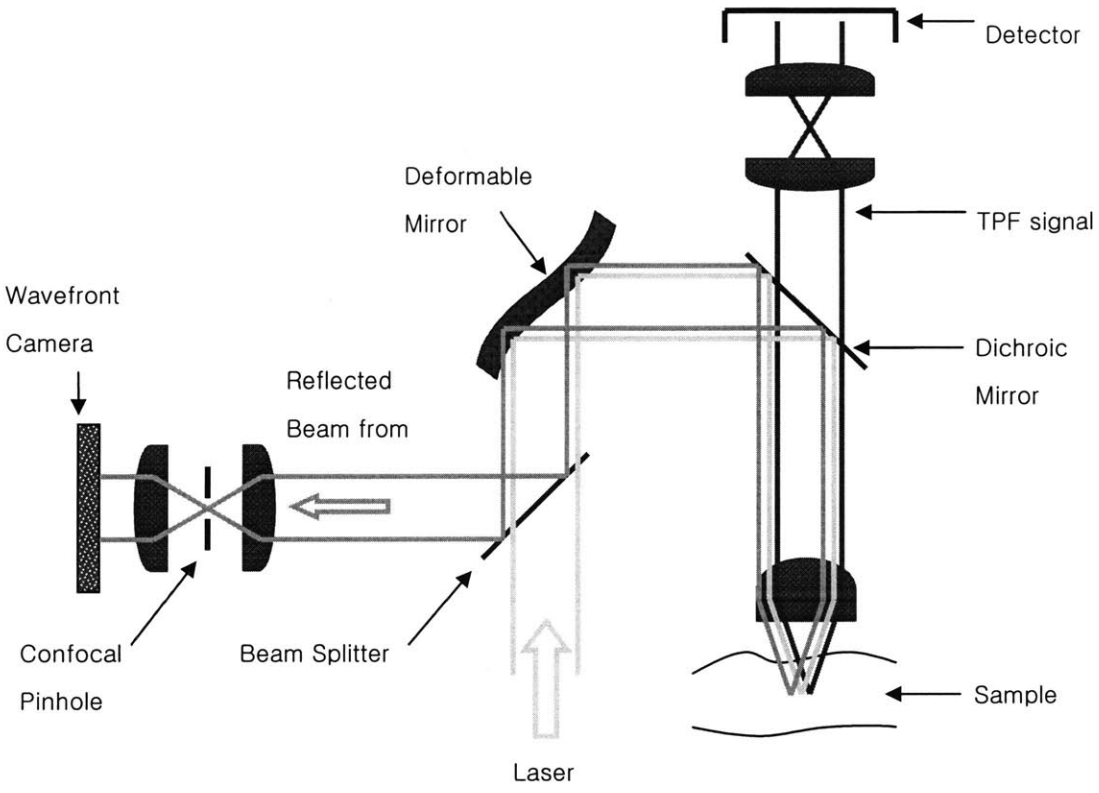

Fig 2.6. System configuration

Fig 2.6 shows our experimental setup, which is a two-photon excitation fluorescence excitation microscope including a wavefront camera, deformable mirror, and confocal system. The excitation laser is coming into the system and is reflected to the two-photon excitation fluorescence microscope by the deformable mirror. Emission fluorescence signal passes the dichroic mirror and reaches a detector, but the reflected light signal goes back along the excitation beam path and finally to the wavefront camera. Before the wavefront camera a confocal pinhole selects only the signal coming from the focal plane. By measuring the wavefront distortion, the wavefront camera gives feedback signal to the deformable mirror. Then, the deformable mirror generates a pre-distortion to the plane wave that counters the distortion induced by the sample. The pre-distortion from the deformable mirror and the distortion from the sample are cancelled out to produce more ideal point spread function at the focal point. More detail is explained later.

2. 2. 4. Confocal pinhole size

The size of the confocal pinhole affects two aspects of the system. A small pinhole is needed to obtain high axial resolution based on confocal principle [9]. However, since the pinhole also acts as a spatial filter, to pass the higher spatial frequency information of the distorted wavefront, a larger pinhole is needed. Therefore, the appropriate size of the pinhole should be determined according to the constraints of the required axial resolution and the required bandwidth of the distorted wavefront spatial frequency.

Fig 2.7 shows the relationship between the pinhole size and the spatial frequency of the distorted wavefront. Let us assume that the shape of the distorted wavefront is *sin kx*. The first lens performs Fourier transform of the *sin kx* and the location of the pinhole is Fourier plane of the first lens. If the pinhole size is smaller than 2k, the information of the distorted wavefront cannot pass, but if the pinhole size is greater than 2k, the information of the distorted wavefront can pass [10]. Therefore, the spatial frequency of the distorted wavefront determines the minimum pinhole size.

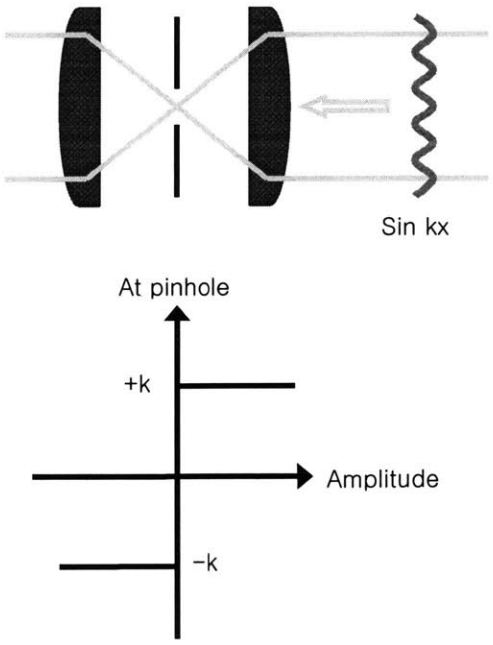

Fig 2.7. Pinhole size

2. 2. 4. 1. Maximum pinhole size from axial resolution

Let us assume that the axial resolution is 1μm, which is the axial resolution of the two-photon excitation fluorescence microscope. Fig 2.8 shows the intensity distribution according to the axial distance and various pinhole sizes assuming unity magnification of the microscope [11].

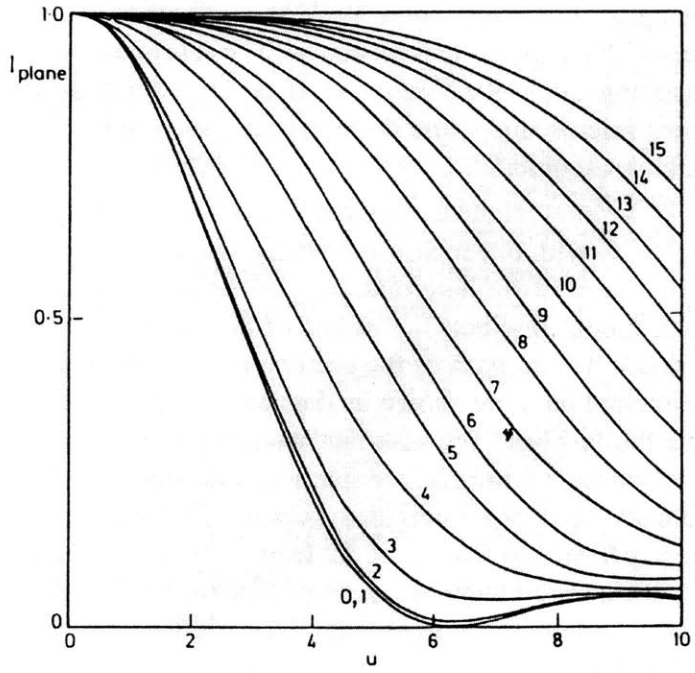

Fig 2.8. Variation of I(u) against u for detector pinhole sizes [11]

In the Fig 2.8, u is normalized axial distance, v_P is normalized radius, and I_{plane} is normalized intensity. The normalized axial distance is defined as

$$u = \frac{8\pi}{\lambda}\sin^2(\alpha/2)z$$

In this equation, z is axial distance and sin α is the numerical aperture (NA) of the objective lens. With 1μm axial resolution and 1.3 NA, u is 3.89. From the Fig 2.8, v_P is 4.17 at the half of the maximum intensity. The normalized radius is defined as

$$v_P = \frac{2\pi}{\lambda}\sin\alpha r_P$$

With v_P and NA, the radius of the pinhole, r_P is calculated at 0.6μm. Therefore, the diameter of the pinhole for the 1μm axial resolution is 1.2μm. I set the diameter to 1μm.

For actual microscope, its magnification is not unity and the pinhole size is magnified by the whole imaging system. Here, the actual system can be modeled as shown in Fig 2.9.

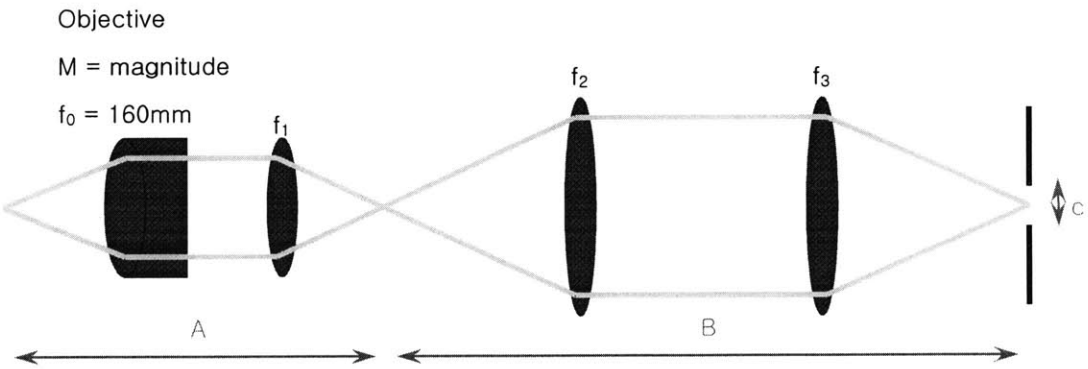

Fig 2.9. Maximum pinhole size

The magnification of A is $M \cdot f_1/f_0$ and the magnification of B is f_3/f_2. Therefore, the magnification of the whole system is $M \cdot (f_1 \cdot f_3)/(f_0 \cdot f_2)$ and f_0 is 160mm. With this equation, the maximum pinhole size, d_{max} is $M \cdot (f_1 \cdot f_3)/(160 \cdot f_2) \cdot 1\mu$m.

2. 2. 4. 2. Minimum pinhole size from wavefront distortion

The largest refractive index difference in a cell is between its nucleus and the cytoplasm [12]. The mean refractive index of a cell is about 1.38, but the refractive index of a nucleus is about 1.59, so the nucleus causes the inhomogeneity of the refractive index and the size of the cell becomes the critical dimension for the wavefront distortion [12]. This gives a critical dimension for wavefront distortion on the order of 10μm, the size of nuclei.

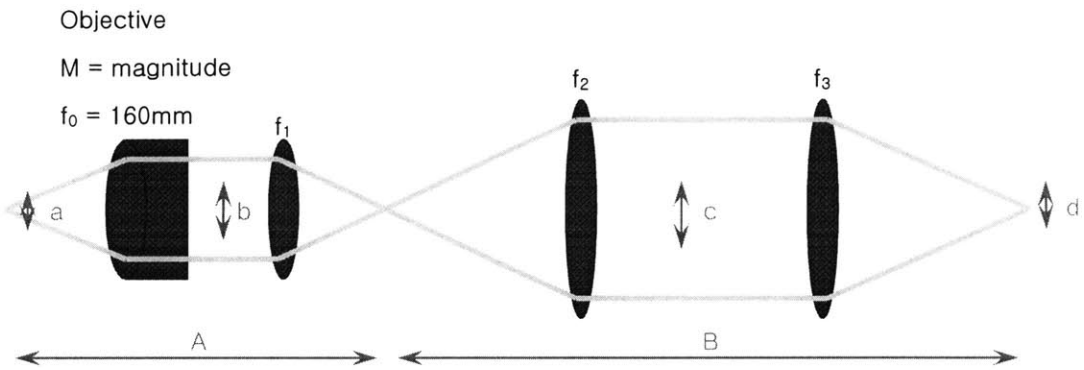

Fig 2.10. Minimum pinhole size

From Fig 2.10, the 10μm objective at position a becomes about 100μm in size at position b because the size of the back aperture of the objective is 10 times larger than the size of the front aperture. 100μm at position b becomes $100\mu m \times f_2/f_1$ at position c and d is Fourier plane of c [10]. Therefore, the minimum pinhole size, d_{min} is

$$d_{min} = 1\mu m \cdot f_3 / (100\mu m \cdot f_2/f_1)\ \mu m \times 1000 = 10 \cdot f_1 \cdot f_3/f_2\ \mu m$$

From the maximum and minimum size of the pinhole,

$$d_{max} = M \cdot (f_1 \cdot f_3)/(160 \cdot f_2) \cdot 1\ \mu m$$

$$d_{min} = 1\mu m \cdot f_3 / (100\mu m \cdot f_2/f_1)\ \mu m \times 1000 = 10 \cdot f_1 \cdot f_3/f_2\ \mu m$$

$$10 \cdot f_1 \cdot f_3/f_2 \leq d \leq M \cdot (f_1 \cdot f_3)/(160 \cdot f_2)$$

$$\therefore M \geq 1600$$

This result shows that for 1μm axial resolution and to pass the distorted wavefront information, the objective whose magnification is greater than 1600 should be used, which is of course not available.

2. 2. 5. Slit detection

From the result of the pinhole size calculation, we cannot use the pinhole to simultaneously obtain required depth discrimination and pass high spatial frequency of wavefront distortion. However, if a slit is used instead of the pinhole, then we can achieve both the axial resolution and passing the wavefront information [13], [Fig 2.11].

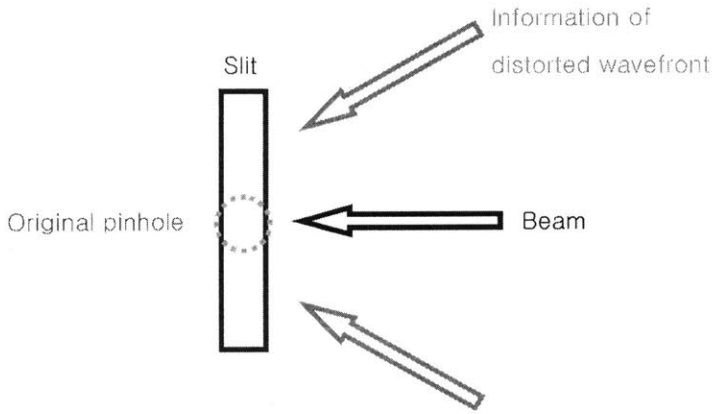

Fig 2.11. Slit detection

However, the slit detection broadens the axial resolution and Fig 2.12 shows the difference of the slit and pinhole detection [14].

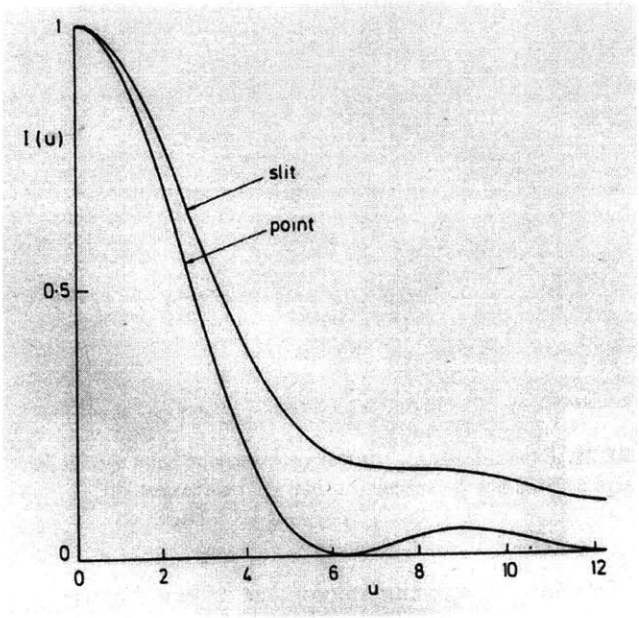

Fig 2.12. Variation of I(u) against u [14]

Even though the axial resolution is broadened, the distorted wavefront information can pass and the confocal system can distinguish the signal from the focal point.

However, the slit detection has limitation. Only one direction of the wavefront information can pass through the slit [Fig 2.13].

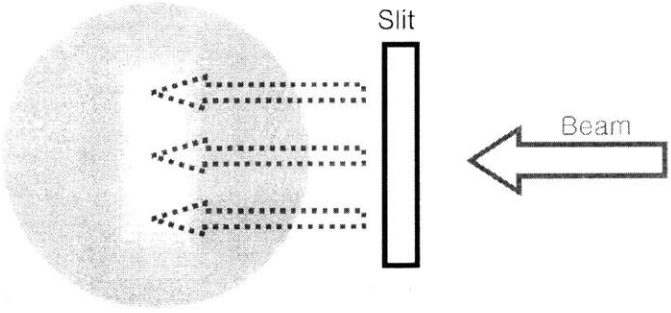

Fig 2.13. Wavefront information passing through a slit

A possible solution is to achieve axial symmetry of wavefront distortion and reconstruct 2D wavefront from a 1D slice [Fig 2.14]. However, wavefront distortion is in general not axial symmetric.

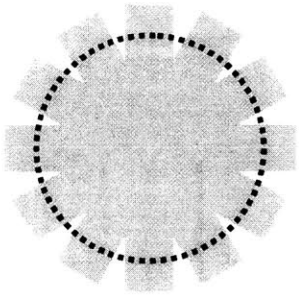

Fig 2.14. Numerically constructed circular area

The second possible solution is to rotate the slit and acquire slices of wavefront distortion in sufficient directions before actuating the deformable mirror for correction

The third solution is to rotate the slit sufficiently fast such that all wavefront information is integrated during one frame of the CCD camera.

2. 3. Strong Background Noise

When the beam passes through a 50/50 beamsplitter, half of the beam goes forward and the rest is reflected to right [Fig 2.15]. However, very small fraction of the beam is reflected inside of the beam splitter and goes left of the beamsplitter and becomes strong background compared with the reflected beam from a sample and ruins S/N ratio.

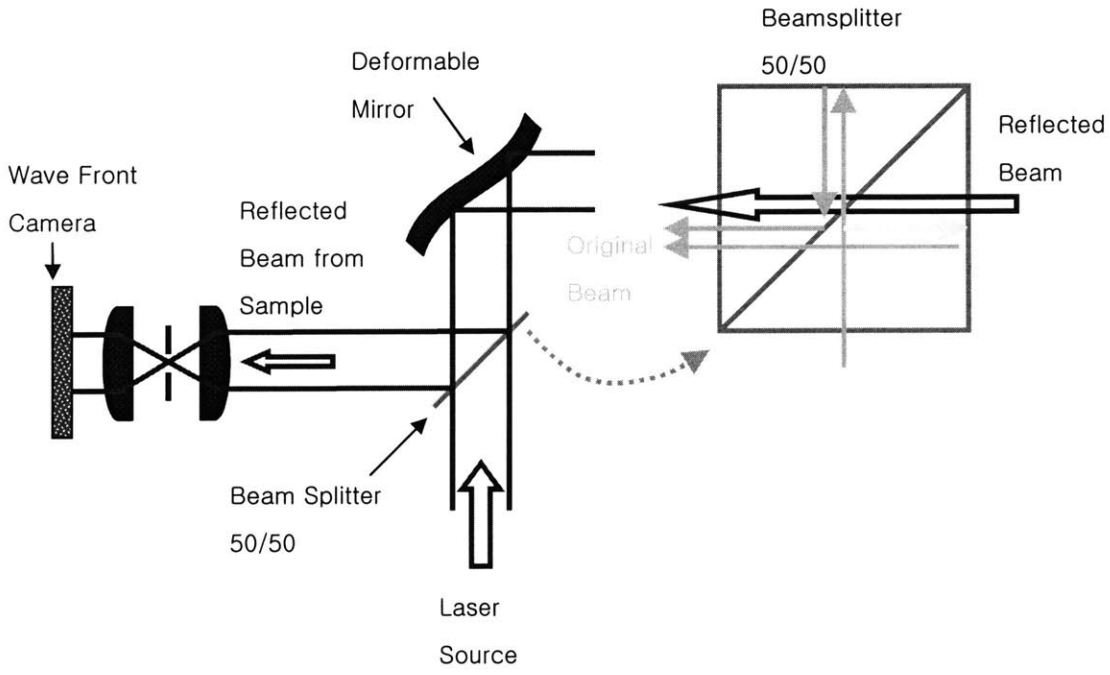

Fig 2.15. Background signal reflected from the beamsplitter

Therefore, I tilted the beam splitter and improved the S/N ratio.

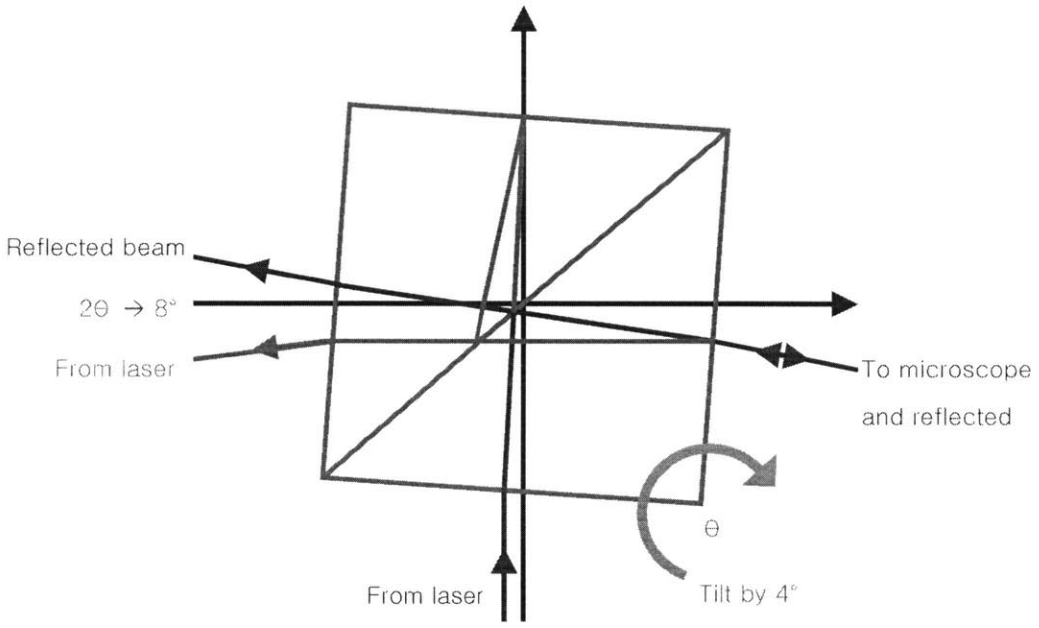

Fig 2.16. Rotation of the beamsplitter

If the beam splitter is rotated by 4° the beam from the laser and the reflected beam from a sample are separated by 8° [Fig 2.16]. First the maximum and minimum intensity of an image was 1000 and 600 and when the system was covered with a black board, it became 1000 and 300. With the tilting method, the intensity became 1000 and 70, which is 330% improvement.

2. 4. Calibrating the wavefront camera and deformable mirror

2. 4. 1. Positions of the wavefront camera and the deformable mirror

Fig 2.17 shows the position of the wavefront camera and the deformable mirror in our system.

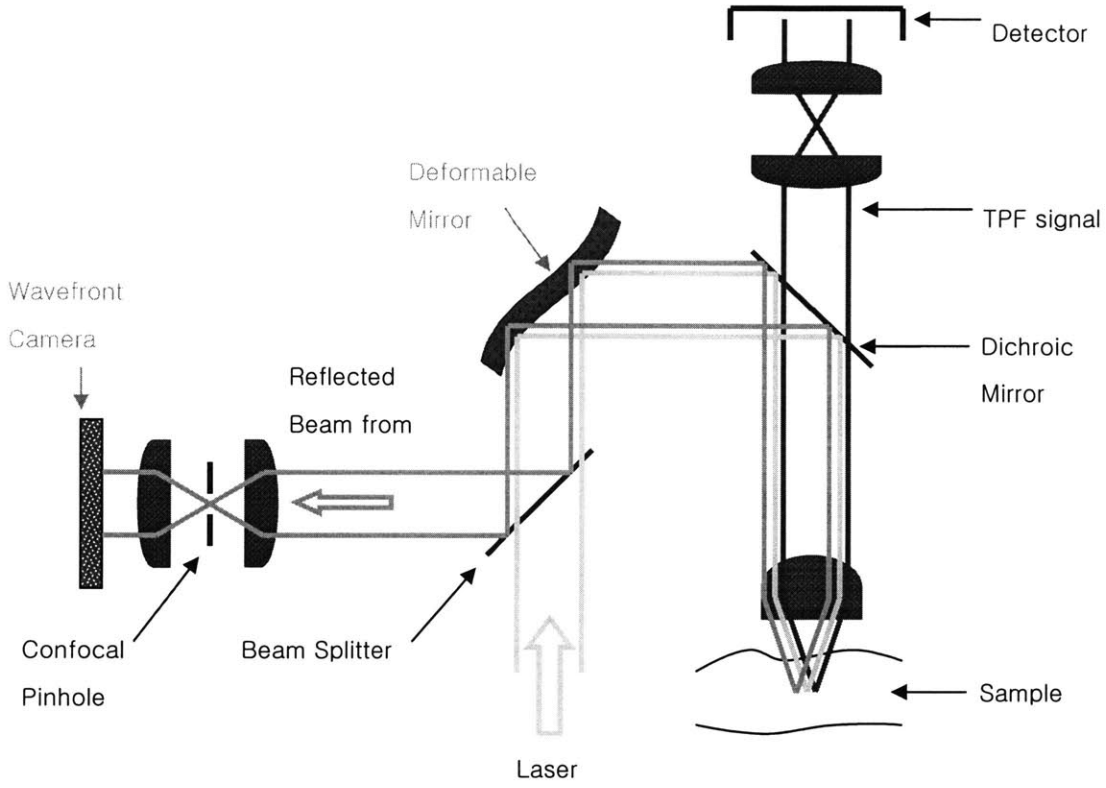

Fig 2.17. the wavefront camera and deformable mirror in the system

The wavefront camera and the deformable mirror should be at conjugate planes. Then one point of the deformable mirror always corresponds to one specific point on the wavefront camera with imaging condition [Fig 2.18].

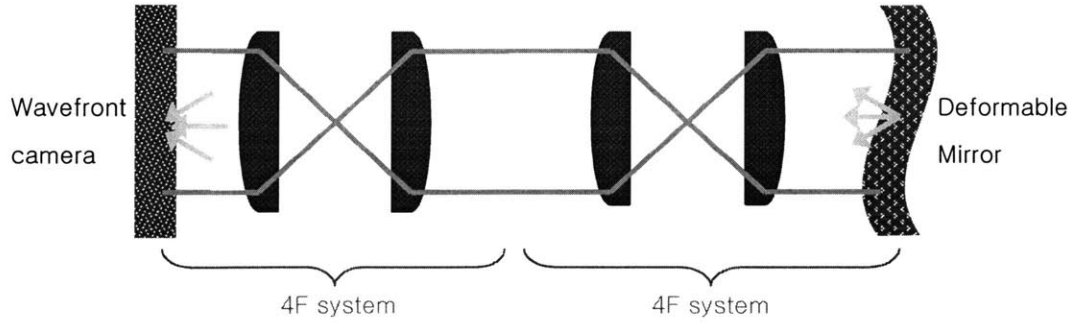

Fig 2.18. The wavefront camera and deformable mirror at conjugate planes

First, let us assume that the deformable mirror has an arbitrary shape and the distorted wavefront is detected at the wavefront camera. Then the wavefront camera gives feedback signal to the deformable mirror to make the wavefront flat [Fig 2.19].

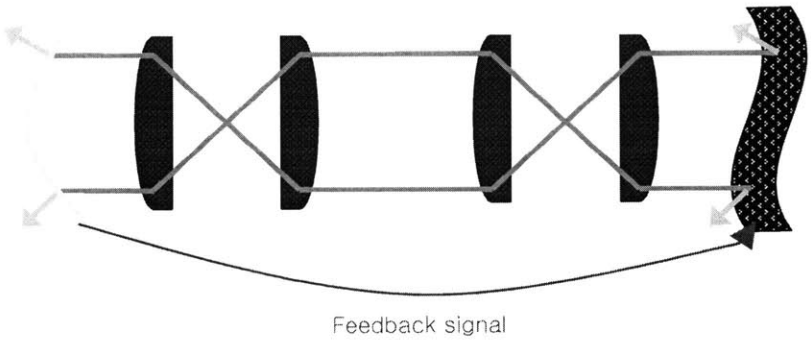

Fig 2.19. Wavefront detection of the wavefront camera

Finally the wavefront becomes flat with closed loop control [Fig 2.20].

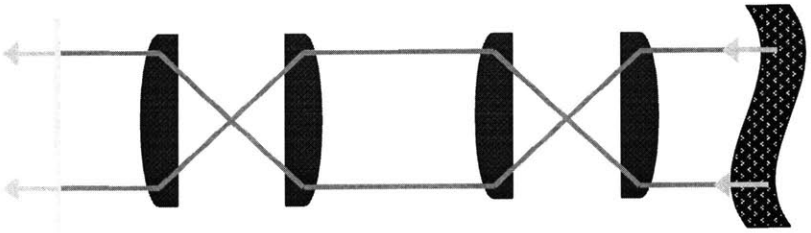

Fig 2.20. Wavefront correction of the deformable mirror

2. 4. 2. Relation between the wavefront camera and the deformable mirror

For the feedback, the relation between the wavefront camera and the deformable mirror should be defined first. The relation can be calculated by interaction matrix and command matrix. The interaction matrix is the wavefront change according to moving actuators and the command matrix is the inverse of the interaction matrix, so the command matrix is used for the feedback signal from the wavefront camera to the deformable mirror [15].

2. 4. 2. 1. Calculating interaction matrix

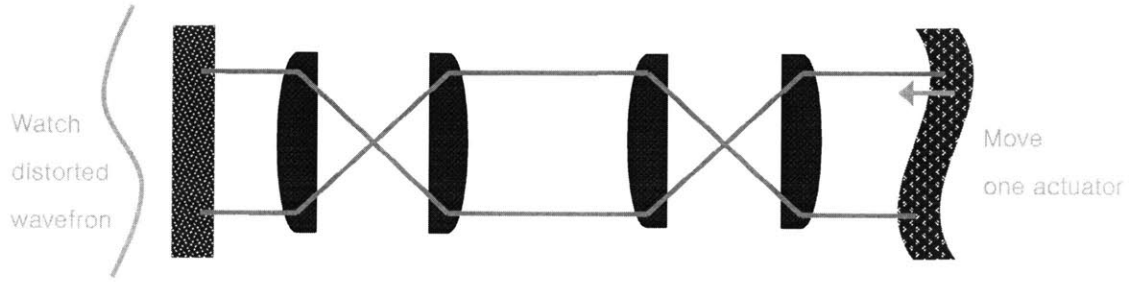

Fig 2.21. Interaction matrix calculation

Interaction matrix is the relationship between applied voltage and wavefront distortion and it is calculated by pushing and pulling all the actuators on the deformable mirror [Fig 2.21]. First, push one actuator on the deformable mirror. Then the wavefront camera detects the sum of wavefront caused by inherent system aberration and one caused by pushing the actuator. Pulling the actuator shows the wavefront camera the sum of wavefront caused by inherent system aberration and one caused by pulling the actuator. Here, the wavefronts by pushing the actuator and pulling the actuator are same magnitude with opposite sign. The half of the difference of the two detected wavefront cancels the inherent system aberration and gives only the wavefront by pushing or pulling one actuator. After testing all 52 actuators on the deformable mirror, the interaction matrix can be calculated regardless of system aberration.

2. 4. 2. 2. Calculating command matrix

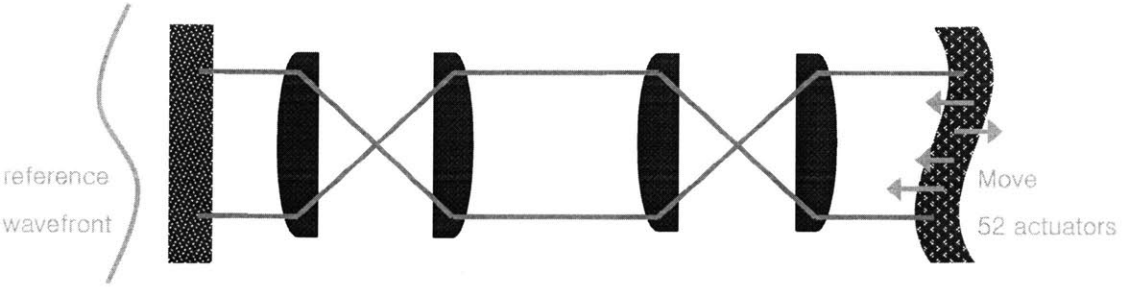

Fig 2.22. Command matrix calculation

Command matrix is the inverse of the interaction matrix. Therefore, the command matrix determines voltages on 52 actuators for correction. Once a reference wavefront is set and a current wavefront is measured, the error between two wavefronts is calculated. The 52 actuators move to make the error zero according to the command matrix [Fig 2.22].

2. 5. Closed loop control for distorted wavefront correction

2. 5. 1. Symmetric sample case

The laser which has flat wavefront comes in and is reflected by the deformable mirror. First the deformable mirror is flat, so the plane wavefront reaches a sample. The sample generates aberration e to the plane wavefront, so the wavefront is distorted and point spread function is broadened. When the reflected beam from the sample goes back to the original beam path, it gets aberration e one more time. The distorted wavefront which has aberration 2e is reflected by the flat deformable mirror and goes to the wavefront camera. The wavefront camera detects the aberration 2e [Fig 2.23].

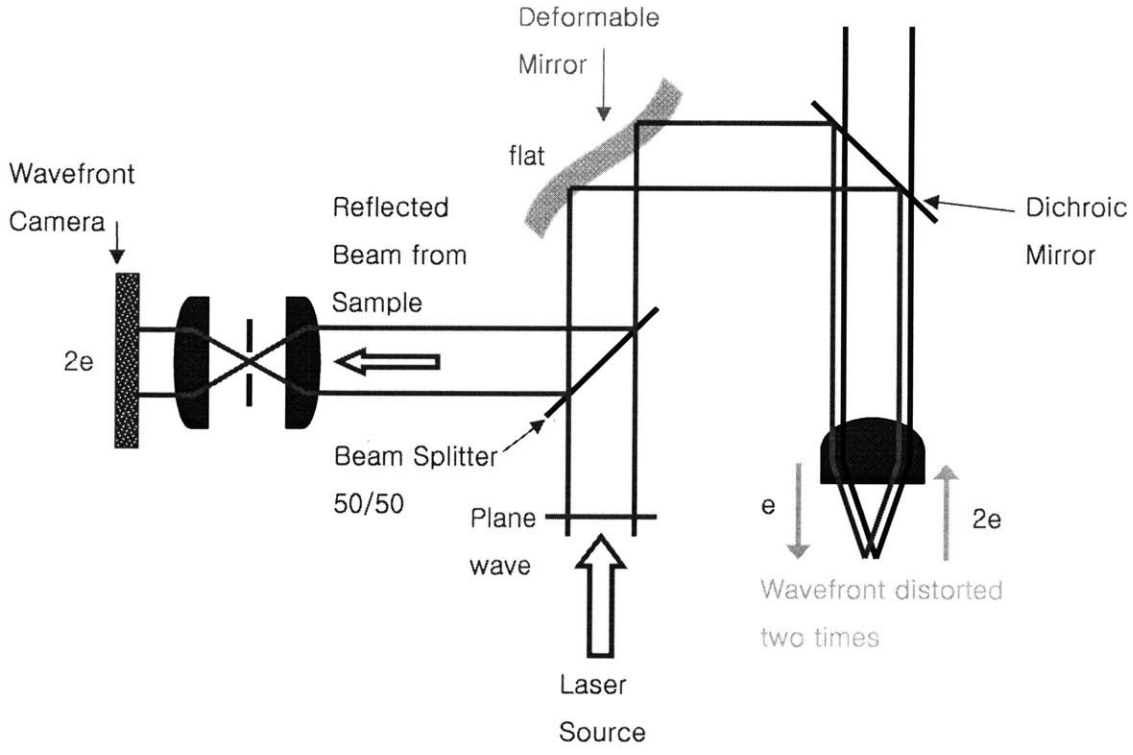

Fig 2.23. Wavefront detection with plane wave

From the previous experiment, the wavefront camera gives –e as feedback signal to the deformable mirror. Let us consider the plane wave going through the system again. The plane wave from the laser is distorted by the deformable mirror in advance and becomes –e. When the distorted wave passes the sample, it gets +e and the aberrations are cancelled out. At the focus ideal point spread function is created. When the beam is reflected to the original beam path, it gets aberration e. However, it is cancelled by the deformable mirror with –e. Finally the wavefront camera sees flat wavefront. Therefore, if the closed loop control runs to get zero error at the wavefront camera, then the ideal point spread function at the focal point is obtained [Fig 2.24].

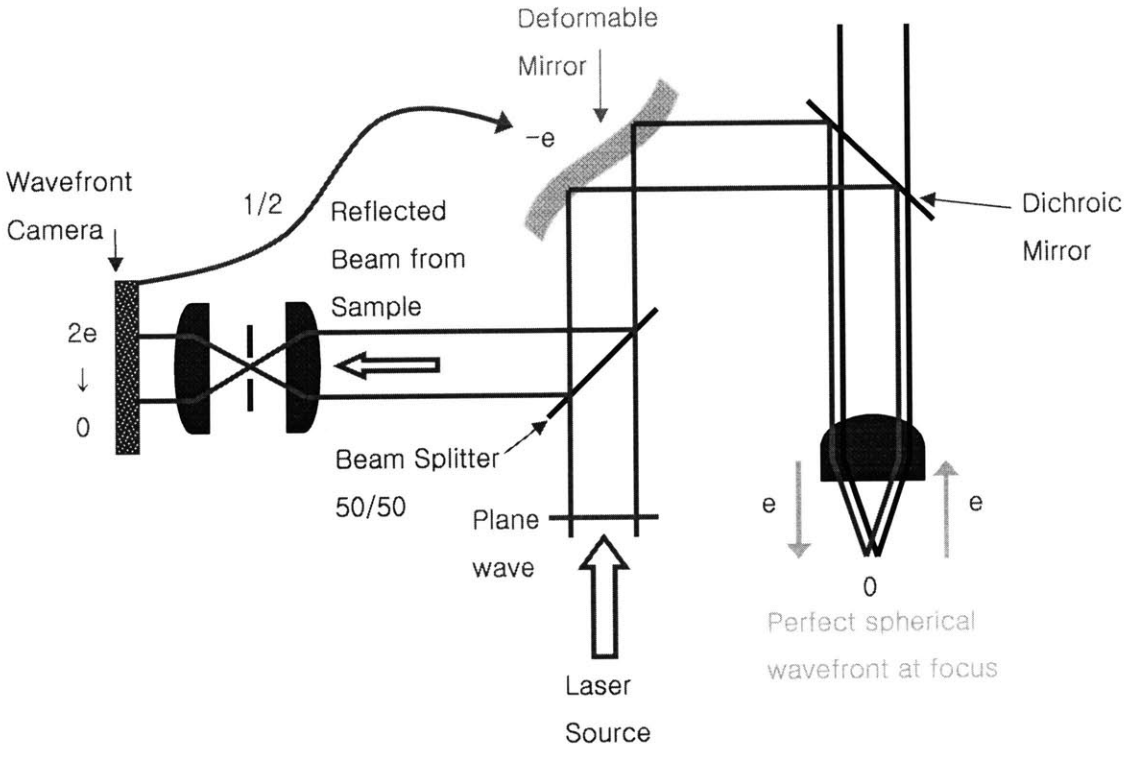

Fig 2.24. Wavefront correction with feedback signal

2. 5. 2. Asymmetric and Highly Scattering Sample Case

Let us assume that a sample generates aberration e only at left part of the sample, the asymmetric case [Fig 2.25]. When the flat wavefront passes a sample, the sample generates aberration e to the left side of the flat wavefront. However, the beam is scattered due to the highly scattering sample and the asymmetric distortion of the wavefront is averaged out. When the scattered beam from the sample goes back to the original beam path, it gets aberration e again only at the left part of the beam [7]. The distorted wavefront is reflected by the flat deformable mirror and goes to the wavefront camera. The wavefront camera detects the aberration e only at the left side.

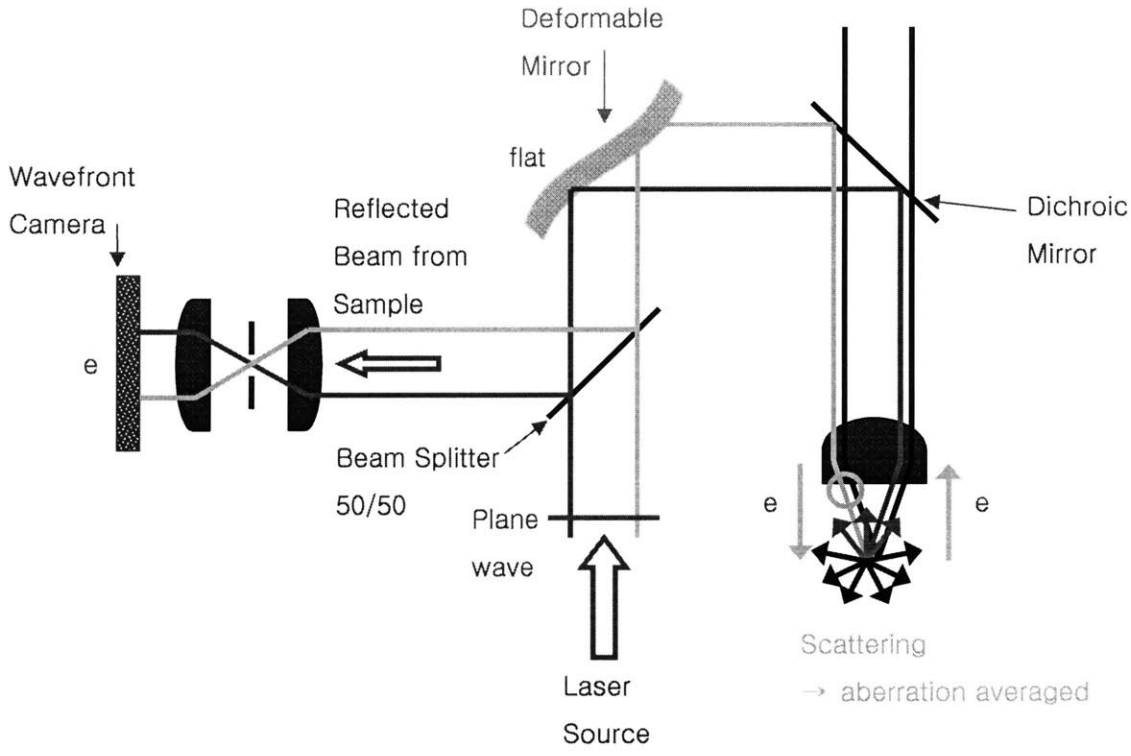

Fig 2.25. Wavefront distortion with asymmetric and highly scattering sample

The wavefront camera gives –e as feedback signal to the right part of the deformable mirror. The plane wave from the laser is distorted by the deformable mirror in advance and becomes –e only at the right side. When the distorted wave passes the sample, it gets +e at the left side and the aberrations are cancelled out. At the focus ideal point spread function is created. When the beam is scattered to the original beam path, it gets aberration e only at the left side. However, it is cancelled by the deformable mirror with –e. Finally the wavefront camera sees flat wavefront. Therefore, if the closed loop control runs to get zero error at the wavefront camera, then the ideal point spread function at the focal point is obtained [Fig 2.26].

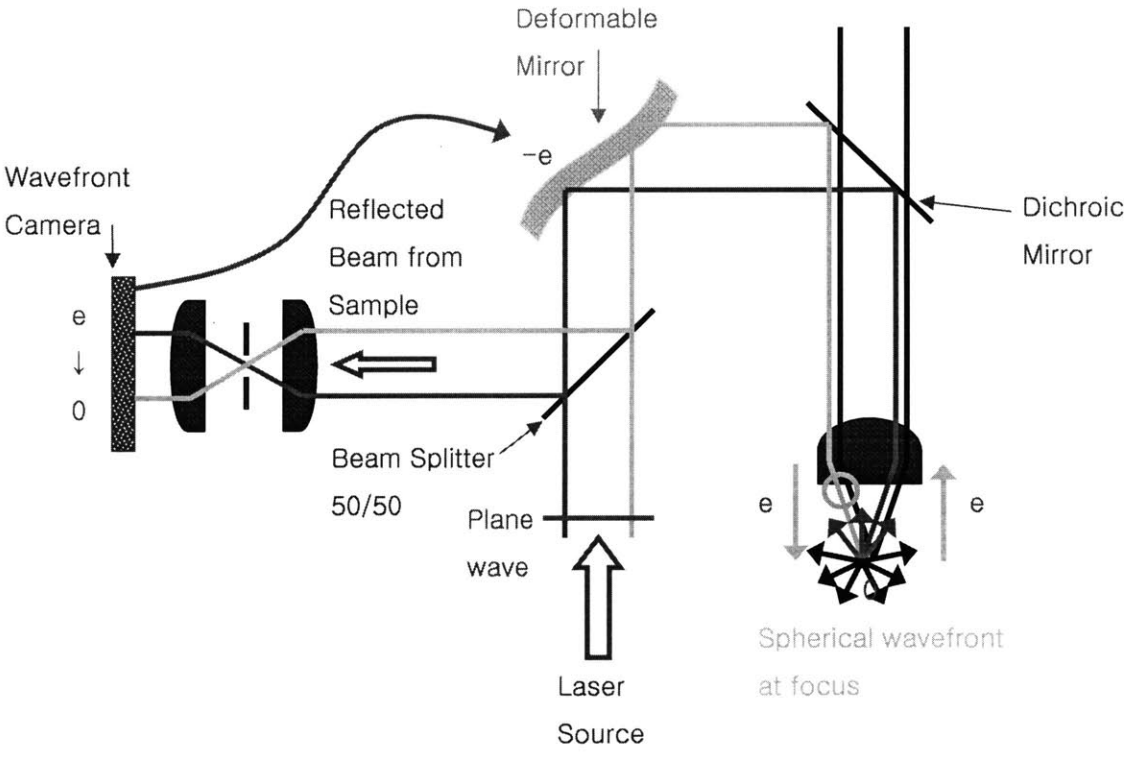

Fig 2.26. Wavefront correction with asymmetric and highly scattering sample

2. 5. 3. Initial aberration from the whole system (symmetric sample case)

Now let us consider the initial aberrations which the whole system may contain. Let us set aberrations e_1, e_2, e_3, and e_4 as Fig 2.27. At the sample, initial system aberration is $e_1+e_2+e_3$. At the wavefront camera, the aberration becomes $e_1+2e_2+2e_3+e_4$. With the feedback signal from the wavefront camera, the wavefront becomes $-\frac{1}{2}(e_1+2e_2+2e_3+e_4)$ at the deformable mirror and $\frac{1}{2}e_1 - \frac{1}{2}e_4$ at the focal point. Therefore, the closed loop holds only when e_1 and e_4 are small.

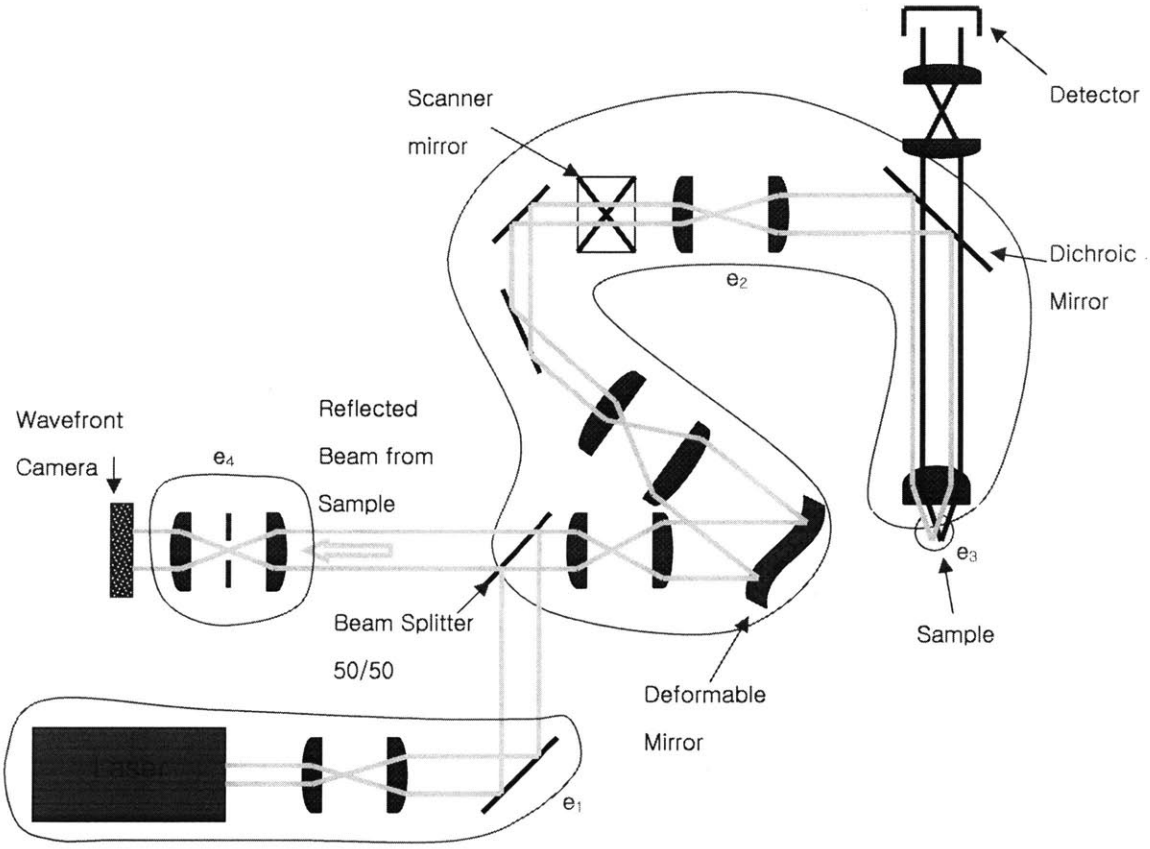

Fig 2.27. Inherent system aberration

2. 5. 3. 1. Aberration at e_1

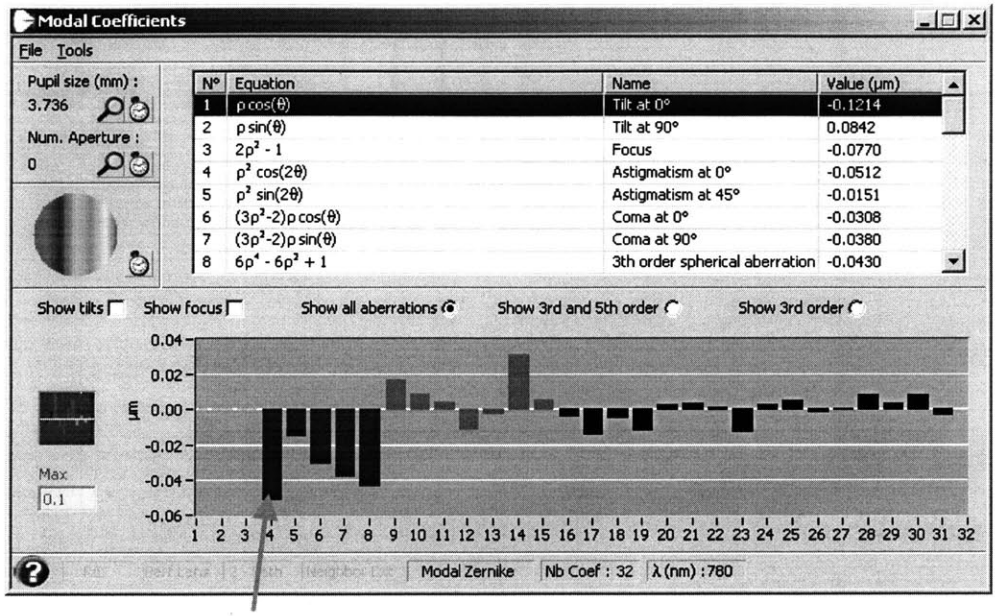

Largest value: 0.051 = 0.065λ

Fig 2.28. Aberrations at e_1

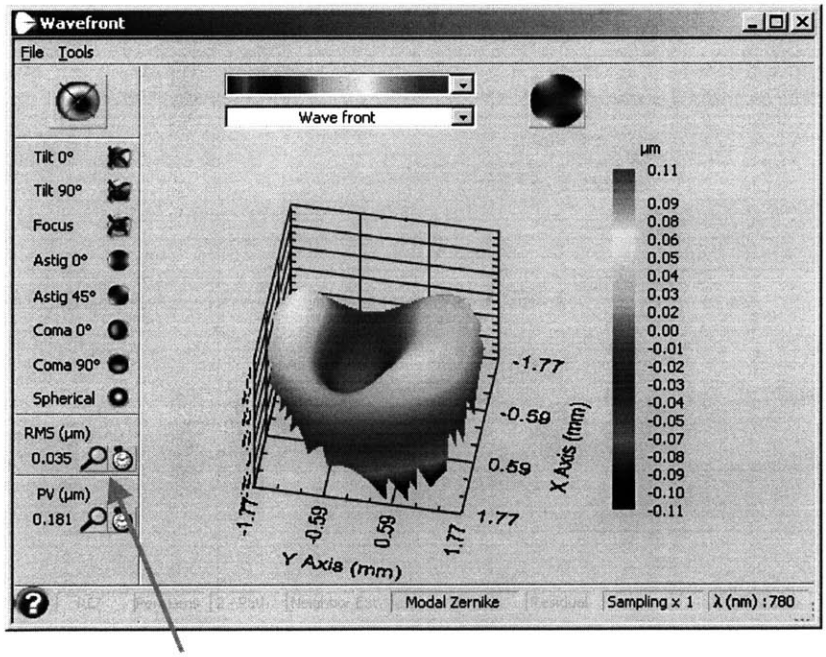

RMS = 0.035 (root mean square of errors between the reference wavefront and measured wavefront)

PV = 0.18 (maximum peak to minimum peak value)

Fig 2.29. Wavefront at e_1

Fig 2.28 and Fig 2.29 shows aberrations and wavefront at e_1. We found that e_1 is smaller than the one adaptive optics system can correct further. In addition, e_4 is smaller than e_1. Therefore, e_1 and e_4 are negligible and the closed loop system holds with these initial aberrations.

2. 6. Detailed system configuration

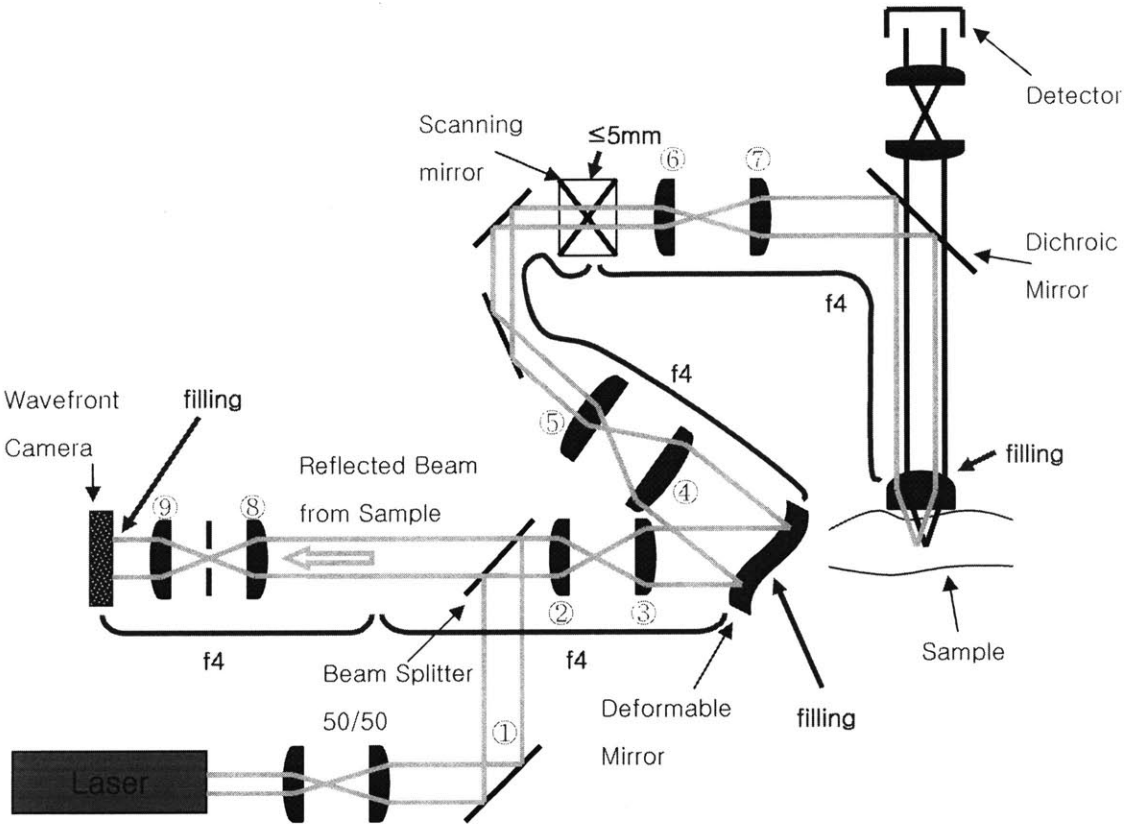

Fig 2.30. System configuration

Fig 2.30 shows detailed system configuration. All pairs of lenses should be at f4 system and the beam should fill the aperture of the wavefront camera, deformable mirror, and the back aperture of the objective lens. The beam size should be smaller than 5mm at the scanning mirrors.

Beam diameter at ①: 6mm

Focal length of lens ②: 100mm

Focal length of lens ③: 200mm

Focal length of lens ④: 400mm

Focal length of lens ⑤: 50mm

Focal length of lens ⑥: 20mm

Focal length of lens ⑦: 125mm

Focal length of lens ⑧: 200mm

Focal length of lens ⑨: 100mm

Distance between lens ② and lens ③: 300mm

Distance between lens ③ and the deformable mirror: 200mm

Distance between the deformable mirror and lens ④: 400mm

Distance between lens ④ and lens ⑤: 450mm

Distance between lens ⑤ and lens ⑥: 70mm

Distance between lens ⑥ and lens ⑦: 145mm

Distance between lens ② and lens ⑧: 300mm

Distance between lens ⑧ and lens ⑨: 300mm

Distance between lens ⑨ and the wavefront camera: 100mm

3. Experiment and Result

3. 1. Signal loss due to spherical aberration as a function of imaging depth

3. 1. 1. Sample generating artificial spherical aberration

This experiment is to measure the signal loss due to spherical aberration as a function of imaging depth. 20x air objective lens and fluorescein sample are used [Fig 3.1]. When the beam is going from the air to the fluorescein sample, spherical aberration is generated due to mismatch of the refractive indices [16]. As the focus goes deeper, the signal loss becomes higher. The signal loss is measured with normal two-photon excitation fluorescence microscope with/without the adaptive optics system and two signal losses are compared. The experiment is performed at 50, 100, 150 micron depths.

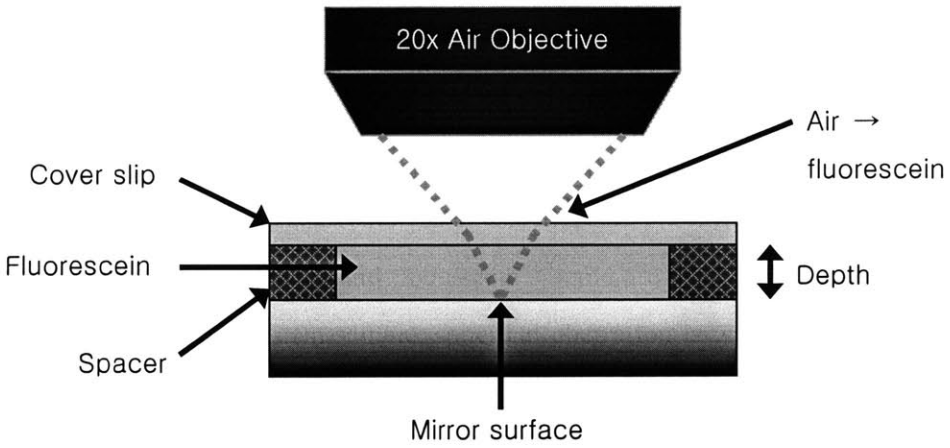

Fig 3.1. Signal loss experiment sample

3. 1. 2. Result

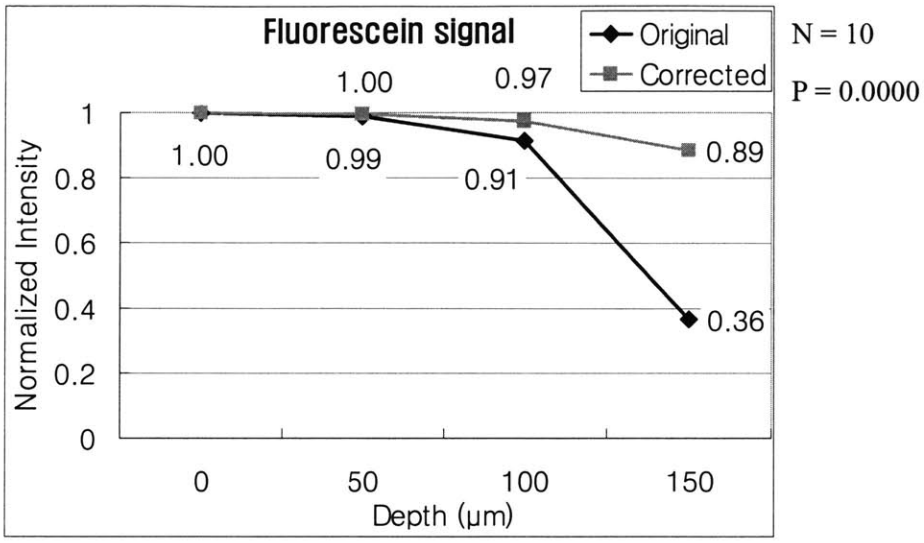

Fig 3.2. Signal loss improvement

Fig 3.2 shows the result of fluorescein emission signal loss experiment. The uncompensated signal is decaying when the focus is going deeper. However, with adaptive optics compensation, the emission signal remains almost flat. The signal improvement is 1% at 50μm, 7% at 100μm, and 143% at 150μm.

Fig 3.3 shows aberration coefficients without compensation and Fig 3.5 shows ones with compensation. Uncompensated maximum aberration is 0.2311μm, but it becomes 0.0495μm with compensation. Spherical aberration becomes 0.0008μm from -0.0173μm.

Fig 3.4 and Fig 3.6 show wavefront change. RMS number becomes 0.043μm from 0.131μm and PV becomes 0.269μm from 0.724μm.

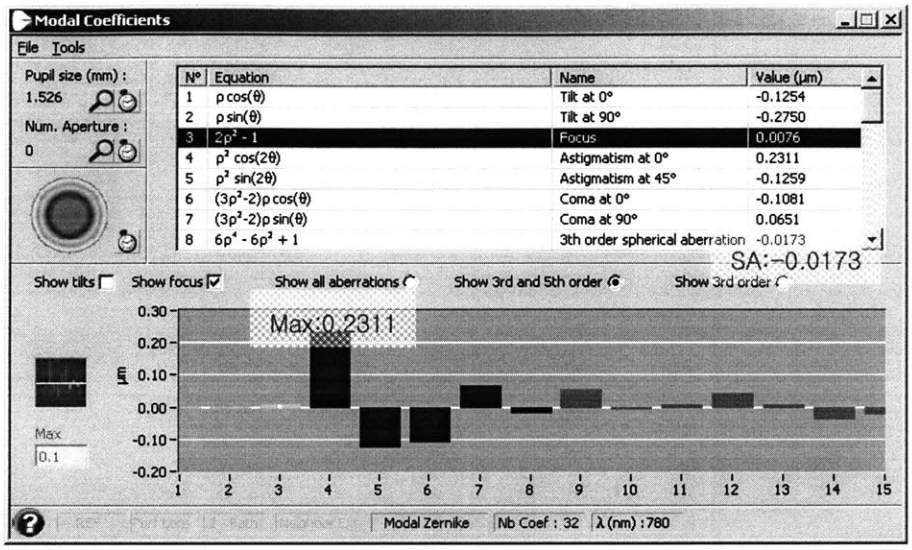

Fig 3.3. Aberration coefficients of uncompensated wavefront

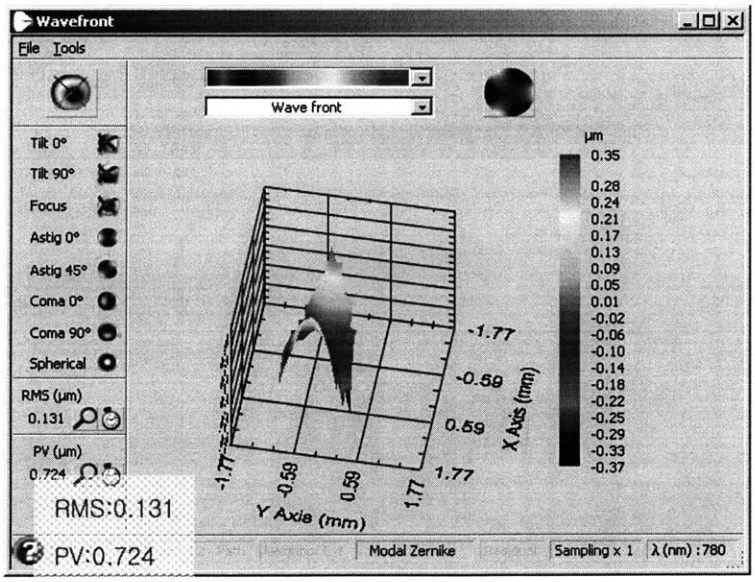

Fig 3.4. Uncompensated wavefront

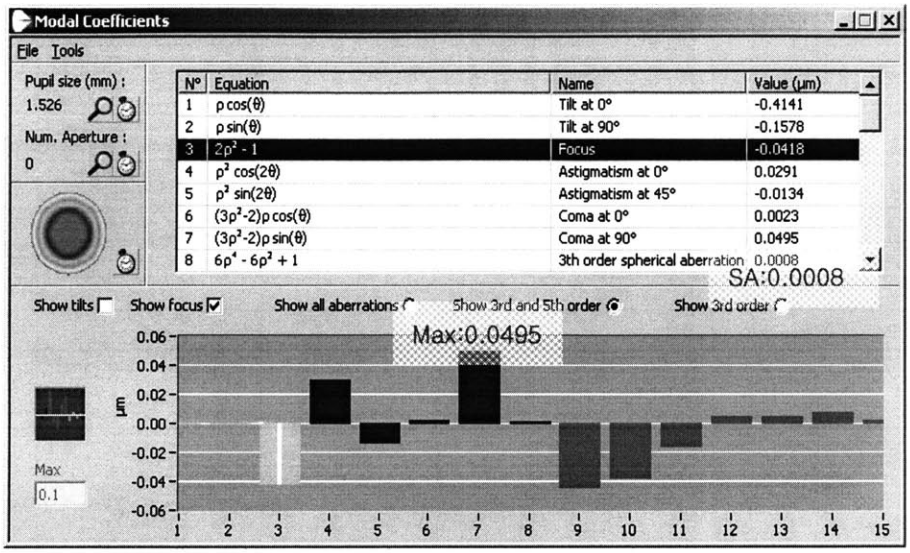

Fig 3.5. Aberration coefficients of compensated wavefront

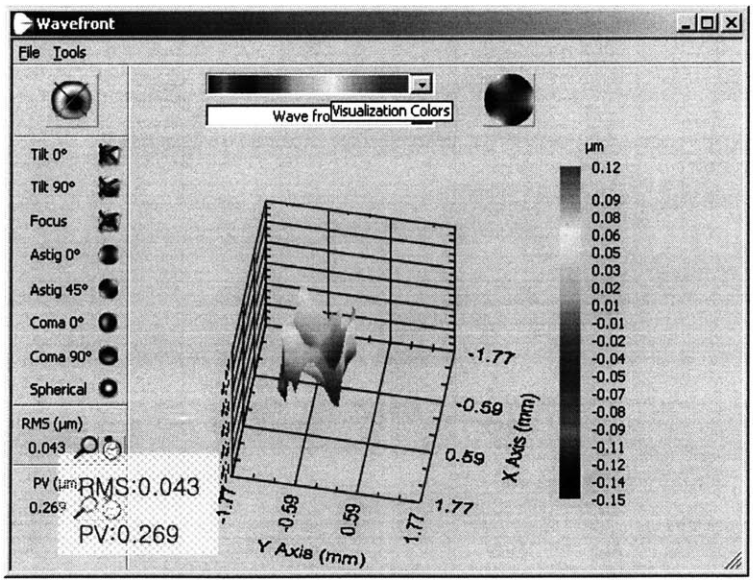

Fig 3.6. Compensated wavefront

3. 2. Point spread function degradation due to spherical aberration as a function of imaging depth

3. 2. 1. Sample generating artificial spherical aberration

This experiment is to measure the point spread function degradation due to spherical aberration as a function of imaging depth. 40x oil immersion objective lens and fluorescence beads are used [Fig 3.7]. When the excitation beam is going from oil to air, spherical aberration is generated due to mismatch of the refractive indices. As the focus goes deeper, the signal loss becomes higher. The point spread function is measured with normal two-photon excitation fluorescence microscope with/without the adaptive optics system and two results are compared. The experiment is performed at 50 micron depths.

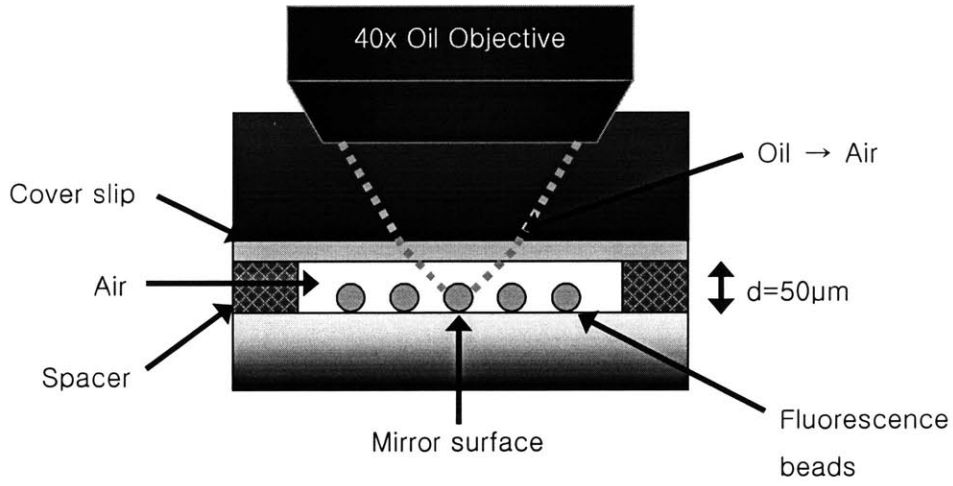

Fig 3.7. PSF degradation experiment sample

3. 2. 2. Result

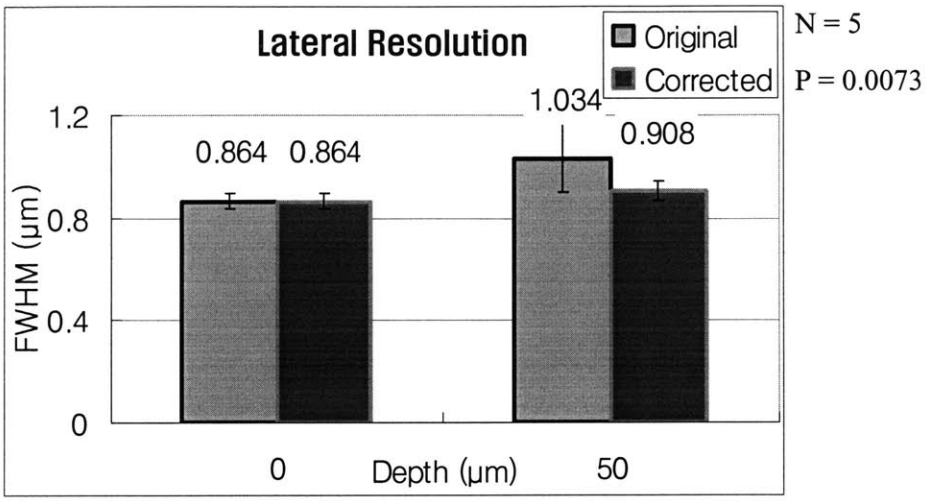

Fig 3.8. Lateral Resolution Improvement

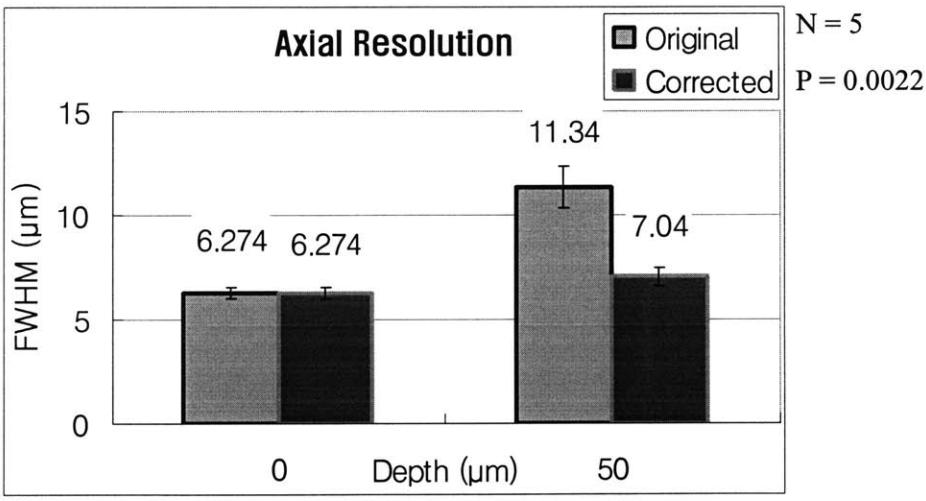

Fig 3.9. Axial Resolution Improvement

Lateral resolution is improved by 14% and axial resolution is improved by 61% [Fig 3.8, Fig 3.9]. Lateral resolution is proportional to 1/NA and Axial resolution is proportional to $1/NA^2$, so it is reasonable result that axial resolution is affected more than lateral resolution with the Adaptive Optics correction.

Fig 3.10 shows aberration coefficients without compensation and Fig 3.12 shows ones with compensation. Uncompensated maximum aberration is -0.4406μm, but it becomes -0.0944μm with correction. Spherical aberration becomes -0.0173μm from -0.1421μm.

Fig 3.11 and Fig 3.13 show wavefront change. RMS number becomes 0.059μm from 0.133μm and PV becomes 0.274μm from 0.758μm.

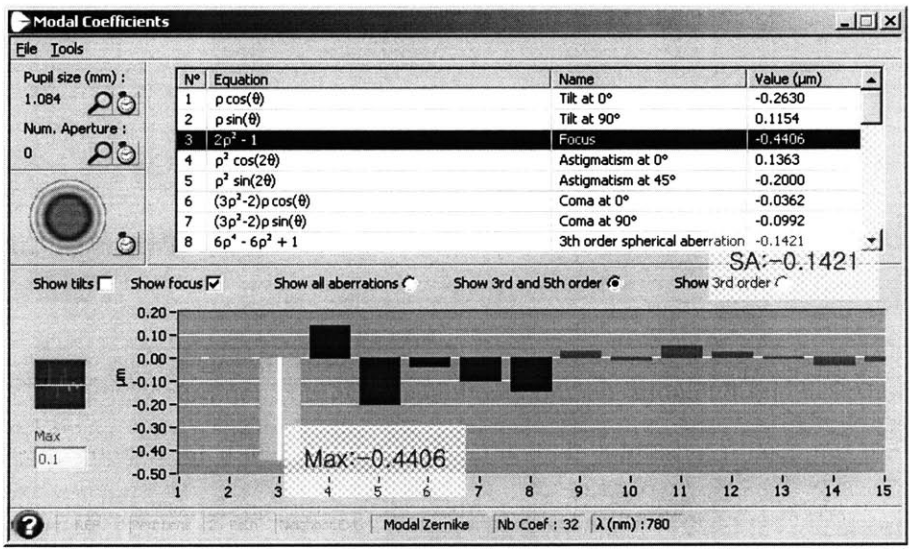

Fig 3.10. Aberration coefficients of uncompensated wavefront

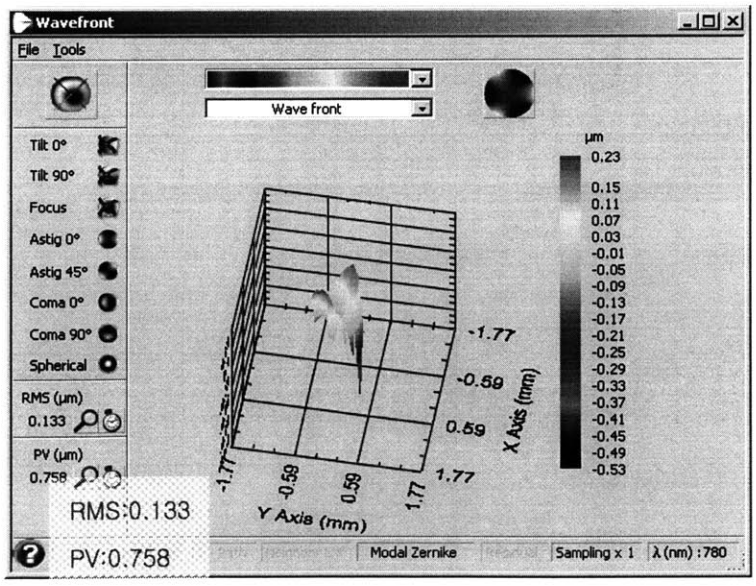

Fig 3.11. Uncompensated wavefront

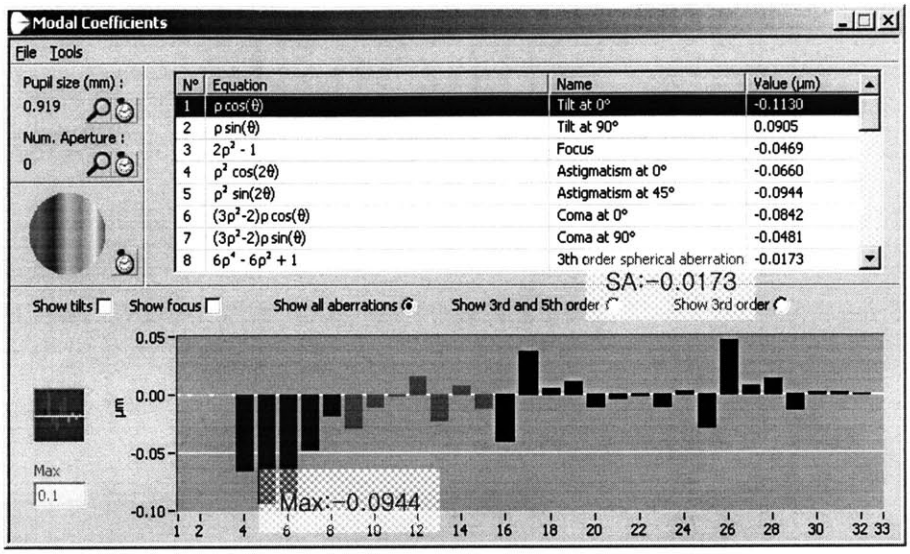

Fig 3.12. Aberration coefficients of compensated wavefront

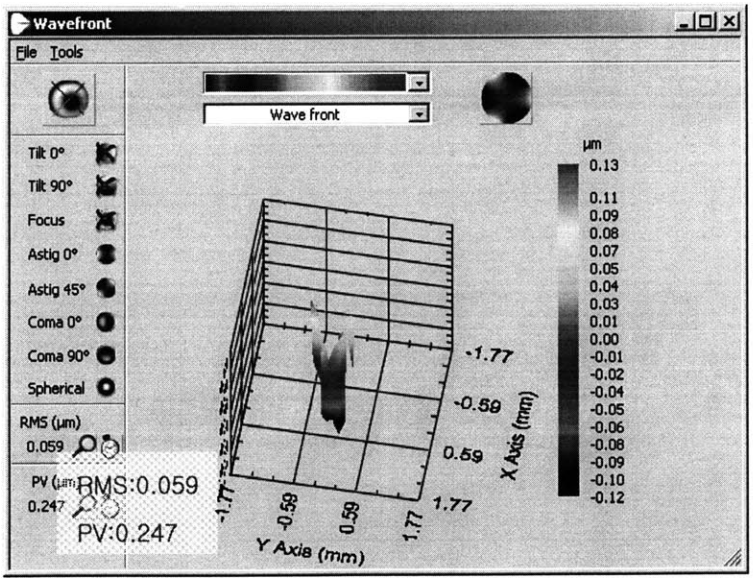

Fig 3.13. Compensated wavefront

4. Conclusion and Future Work

Wavefront distortion by inhomogeneous samples can be measured by a Shark-Hartmann wavefront sensor and a reflected light confocal system and corrected by a deformable mirror. By using the reflected light confocal system and the Shack-Hartmann wavefront sensor, wavefront distortion can be detected without scanning in the reference arm. Emission signal improvement is 1 to 143% in 50 to 150μm depth and the axial resolution improvement is 63% in 50μm depth.

So far I achieved the improvement with fluorescein and bead samples. The next task is to apply the adaptive optics to image biological samples. However the current problem is that the reflected signal from the sample is very weak compared to background noise signal. One of the background noise signals, which is signal from out-of-focus planes, was mentioned and solved. The other signal is due to the reflection from each optical component. For example, a lens gives a small amount of reflection, but compared to the reflected signal from the sample, it is quite strong. The possible solution is to use a polarizer. The reflection has certain polarization direction, so using a polarizer it is expected to get rid of the background signal. The next step is to combine the adaptive optics system to a microscope which uses long wavelength excitation. Using long wavelength, we can go deeper and the adaptive optics is expected to have more impact on the long wavelength excitation microscope.

5. References

1. Göppert-Mayer, M., *Uber Elementarakte mit zwei Quantensprungen.* Ann. Phys, 1931. **9**: p. 273-295.
2. So, P.T.C., et al., *Two-photon excitation fluorescence microscopy.* Annual Review of Biomedical Engineering, 2000. **2**: p. 399-429.
3. Denk, W., J.H. Strickler, and W.W. Webb, *2-Photon Laser Scanning Fluorescence Microscopy.* Science, 1990. **248**(4951): p. 73-76.
4. Rigaut, F., et al., *Adaptive Optics on a 3.6-M Telescope - Results and Performance.* Astronomy and Astrophysics, 1991. **250**(1): p. 280-290.
5. Liang, J.Z., D.R. Williams, and D.T. Miller, *High resolution imaging of the living human retina with adaptive optics.* Investigative Ophthalmology & Visual Science, 1997. **38**(4): p. 55-55.
6. Feierabend, M., M. Rueckel, and W. Denk, *Coherence-gated wave-front sensing in strongly scattering samples.* Optics Letters, 2004. **29**(19): p. 2255-2257.
7. Rueckel, M., J.A. Mack-Bucher, and W. Denk, *Adaptive wavefront correction in two-photon microscopy using coherence-gated wavefront sensing.* Proceedings of the National Academy of Sciences of the United States of America, 2006. **103**(46): p. 17137-17142.
8. *Welcome to the HASO world.* 2006: Imagine Optic.
9. Sandison, D.R. and W.W. Webb, *Background Rejection and Signal-to-Noise Optimization in Confocal and Alternative Fluorescence Microscopes.* Applied Optics, 1994. **33**(4): p. 603-615.
10. Goodman, J.W., *Introduction To Fourier Optics*. 2004: Roberts & Co.
11. Wilson, T. and A.R. Carlini, *Size of the Detector in Confocal Imaging-Systems.* Optics Letters, 1987. **12**(4): p. 227-229.
12. Beuthan, J., et al., *The spatial variation of the refractive index in biological cells.* Physics in Medicine and Biology, 1996. **41**(3): p. 369-382.
13. Sheppard, C.J.R. and X.Q. Mao, *Confocal Microscopes with Slit Apertures.* Journal of Modern Optics, 1988. **35**(7): p. 1169-1185.
14. Wilson, T., *Optical Sectioning in Confocal Fluorescent Microscopes.* Journal of Microscopy-Oxford, 1989. **154**: p. 143-156.
15. Porter, J., *Adaptive Optics for Vision Science: Principles, Practices, Design, and Applications*. 2006: Wiley-Interscience.
16. Fwu, P.T., et al., *Effects of index-mismatch-induced spherical aberration in pump-probe*

microscopic image formation. Applied Optics, 2005. **44**(20): p. 4220-4227.

17. *mirao52d deformable mirror*. 2006: Imagine Optic.

6. Appendix

6. 1. Shark-Hartmann wavefront sensor

Fig 6.1 is the Shark-Hartmann wavefront sensor which I used.

Fig 6.1. Shark-Hartmann wavefront sensor [8]

Its aperture is 3.6×3.6 mm^2 and the number of sub-apertures is 32×32. Maximum tilt dynamic range ± 3° and processing frequency is 4 to 20 Hz [8].

6. 2. Deformable mirror

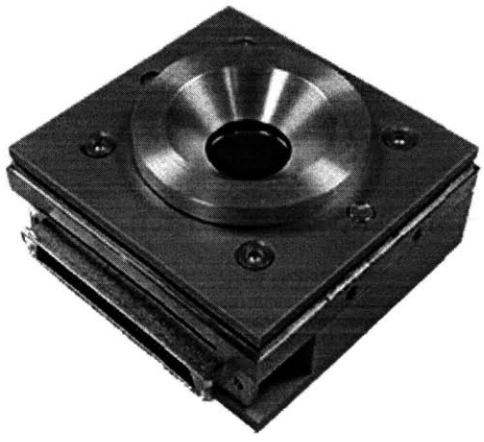

Fig 6.2. Deformable mirror [17]

Fig 6.2 shows the deformable mirror. The number of actuators is 52 and maximum PV which can be generated is 50μm. The mirror surface is coated with silver and its pupil diameter is 15 mm. Maximum bandwidth is 250 Hz [17].

Fig 6.3 shows the examples of several modes which the deformable mirror can make.

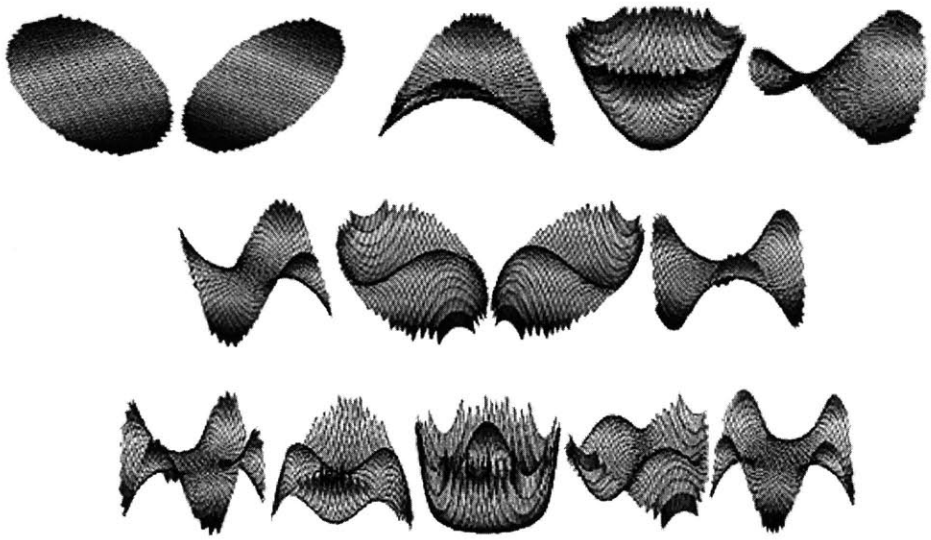

Fig 6.3. Several modes of the deformable mirror [17]

6. 3. Resolution of the current system

In the current system, the back aperture of the objective is not overfilled to get the same diameter of the reflected beam as that of the input beam. Because of it, the numerical aperture becomes smaller than the full numerical aperture of the objective (40× oil immersion, NA 1.3). By measuring the lateral and axial resolution, the numerical aperture is calculated and it is 0.55. The lateral resolution is 0.86μm [Fig 6.4] and axial resolution is 6.27μm. The resolution is measured with 0.1μm fluorescence bead and 780nm, 200mW laser.

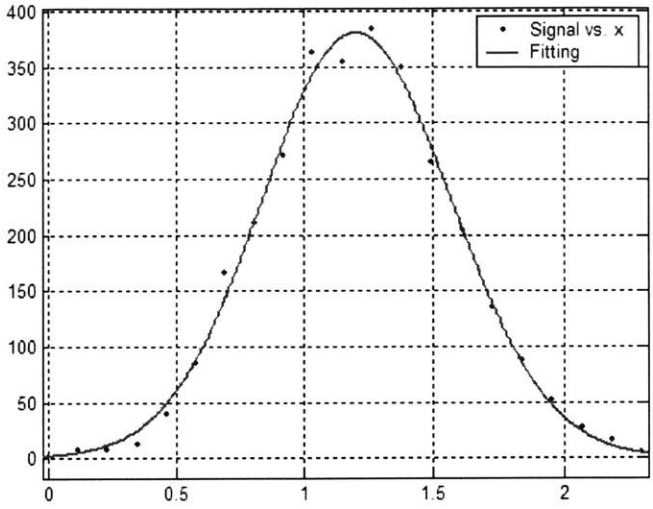

Fig 6.4. Lateral resolution of the current system